LJMU Research Online

Laskar, T, Alexander, KD, Margutti, R, Eftekhari, T, Chornock, R, Berger, E, Cendes, Y, Duerr, A, Perley, DA, Ravasio, ME, Yamazaki, R, Ayache, EH, Barclay, T, Duran, RB, Bhandari, S, Brethauer, D, Christy, CT, Coppejans, DL, Duffell, P, Fong, WF, Gomboc, A, Guidorzi, C, Kennea, JA, Kobayashi, S, Levan, A, Lobanov, AP, Metzger, BD, Ros, E, Schroeder, G and Williams, PKG

 The Radio to GeV Afterglow of GRB 221009A

http://researchonline.ljmu.ac.uk/id/eprint/19858/

Article

CrossMark

The Radio to GeV Afterglow of GRB 221009A

Tanmoy Laskar[1,2], Kate D. Alexander[3], Raffaella Margutti[4], Tarraneh Eftekhari[5,6,31], Ryan Chornock[7], Edo Berger[8], Yvette Cendes[8], Anne Duerr[1], Daniel A. Perley[9], Maria Edvige Ravasio[2,10], Ryo Yamazaki[11,12], Eliot H. Ayache[13], Thomas Barclay[14,15], Rodolfo Barniol Duran[16], Shivani Bhandari[17,18,19,20], Daniel Brethauer[7], Collin T. Christy[3], Deanne L. Coppejans[21], Paul Duffell[22], Wen-fai Fong[5,6], Andreja Gomboc[23], Cristiano Guidorzi[24,25,26], Jamie A. Kennea[27], Shiho Kobayashi[9], Andrew Levan[2], Andrei P. Lobanov[28], Brian D. Metzger[29,30], Eduardo Ros[28], Genevieve Schroeder[5,6], and P. K. G. Williams[8]

[1] Department of Physics & Astronomy, University of Utah, Salt Lake City, UT 84112, USA
[2] Department of Astrophysics/IMAPP, Radboud University, P.O. Box 9010, 6500 GL, Nijmegen, The Netherlands
[3] Department of Astronomy/Steward Observatory, 933 North Cherry Avenue, Rm. N204, Tucson, AZ 85721-0065, USA
[4] Department of Astronomy and Physics, University of California, 501 Campbell Hall, Berkeley, CA 94720-3411, USA
[5] Department of Physics and Astronomy, Northwestern University, 2145 Sheridan Road, Evanston, IL 60208-3112, USA
[6] Center for Interdisciplinary Exploration and Research in Astrophysics, 1800 Sherman Avenue, Evanston, IL 60201, USA
[7] Department of Astronomy, University of California, 501 Campbell Hall, Berkeley, CA 94720-3411, USA
[8] Center for Astrophysics | Harvard & Smithsonian, Cambridge, MA 02138, USA
[9] Astrophysics Research Institute, Liverpool John Moores University, IC2, Liverpool Science Park, 146 Brownlow Hill, Liverpool, L3 5RF, UK
[10] INAF–Astronomical Observatory of Brera, via E. Bianchi 46, I-23807 Merate, Italy
[11] Department of Physical Sciences, Aoyama Gakuin University, 5-10-1 Fuchinobe, Sagamihara 252-5258, Japan
[12] Institute of Laser Engineering, Osaka University, 2-6 Yamadaoka, Suita, Osaka 565-0871, Japan
[13] The Oskar Klein Centre, Department of Astronomy, Stockholm University, AlbaNova, SE-106 91 Stockholm, Sweden
[14] NASA Goddard Space Flight Center, Greenbelt, MD 20771, USA
[15] University of Maryland, Baltimore County, 1000 Hilltop Cir, Baltimore, MD 21250, USA
[16] Department of Physics and Astronomy, California State University, 6000 J Street, Sacramento, CA 95819-6041 USA
[17] ASTRON, Netherlands Institute for Radio Astronomy, Oude Hoogeveensedijk 4, NL-7991 PD Dwingeloo, The Netherlands
[18] Joint institute for VLBI ERIC, Oude Hoogeveensedijk 4, NL-7991 PD Dwingeloo, The Netherlands
[19] Anton Pannekoek Institute for Astronomy, University of Amsterdam, Science Park 904, NL-1098 XH Amsterdam, The Netherlands
[20] CSIRO, Space and Astronomy, P.O. Box 76, Epping, NSW 1710 Australia
[21] Department of Physics, University of Warwick, Coventry, CV4 7AL, UK
[22] Department of Physics and Astronomy, Purdue University, 525 Northwestern Avenue, West Lafayette, IN 47907, USA
[23] Center for Astrophysics and Cosmology, University of Nova Gorica, Vipavska 11c, 5270 Ajdovščina, Slovenia
[24] Department of Physics and Earth Science, University of Ferrara, Via Saragat 1, I-44122 Ferrara, Italy
[25] INFN—Sezione di Ferrara, Via Saragat 1, I-44122 Ferrara, Italy
[26] INAF—Osservatorio di Astrofisica e Scienza dello Spazio di Bologna, Via Piero Gobetti 101, I-40129 Bologna, Italy
[27] Department of Astronomy and Astrophysics, The Pennsylvania State University, 525 Davey Lab, University Park, PA 16802, USA
[28] Max-Planck-Institut für Radioastronomie, Auf dem Hügel 69, D-53121 Bonn, Germany
[29] Department of Physics and Columbia Astrophysics Laboratory, Columbia University, Pupin Hall, New York, NY 10027, USA
[30] Center for Computational Astrophysics, Flatiron Institute, 162 5th Ave, New York, NY 10010, USA

Abstract

GRB 221009A ($z = 0.151$) is one of the closest known long γ-ray bursts (GRBs). Its extreme brightness across all electromagnetic wavelengths provides an unprecedented opportunity to study a member of this still-mysterious class of transients in exquisite detail. We present multiwavelength observations of this extraordinary event, spanning 15 orders of magnitude in photon energy from radio to γ-rays. We find that the data can be partially explained by a forward shock (FS) from a highly collimated relativistic jet interacting with a low-density, wind-like medium. Under this model, the jet's beaming-corrected kinetic energy ($E_K \sim 4 \times 10^{50}$ erg) is typical for the GRB population. The radio and millimeter data provide strong limiting constraints on the FS model, but require the presence of an additional emission component. From equipartition arguments, we find that the radio emission is likely produced by a small amount of mass ($\lesssim 6 \times 10^{-7}$ $M_\odot$) moving relativistically ($\Gamma \gtrsim 9$) with a large kinetic energy ($\gtrsim 10^{49}$ erg). However, the temporal evolution of this component does not follow prescriptions for synchrotron radiation from a single power-law distribution of electrons (e.g., in a reverse shock or two-component jet), or a thermal-electron population, perhaps suggesting that one of the standard assumptions of afterglow theory is violated. GRB 221009A will likely remain detectable with radio telescopes for years to come, providing a valuable opportunity to track the full lifecycle of a powerful relativistic jet.

Unified Astronomy Thesaurus concepts: High energy astrophysics (739); Gamma-ray bursts (629)

Supporting material: machine-readable tables

---

[31] NHFP Einstein Fellow.

1. Introduction

Long-duration γ-ray bursts (GRBs) release enormous amounts of energy in the form of collimated, highly relativistic jets. These outflows are thought to be launched by a powerful magnetar or accreting black hole born during the collapse of a

massive star (Piran 2005; Woosley & Bloom 2006; Marshall et al. 2011). GRBs are typically discovered via their prompt (seconds-to-minutes duration) γ-ray emission, possibly powered by internal shocks within the jet (Rees & Meszaros 1992; Kobayashi et al. 1997; Kumar & Piran 2000). The properties of the jet, such as its structure, energetics, and magnetization, along with other physically interesting quantities such as the structure and density of the ambient medium can be derived from modeling the broadband afterglow emission, which typically remains detectable in the radio, optical, and X-ray bands for days to months (e.g., Sari et al. 1998).

Synchrotron models, based on both analytical and numerical or hydrodynamic calculations, have been remarkably successful in explaining the multiwavelength afterglow emission of GRBs. In the basic picture, the afterglow is modeled as synchrotron radiation produced by a population of relativistic electrons accelerated in the forward shock (FS) produced by the interaction of the jet with the ambient medium. The radiating electrons are assumed to be accelerated into a single power-law distribution of energies, characterized by a minimum energy, $\gamma_m m_e c^2$, and a power-law index, p. This creates a simple broken power-law emission spectrum, fully characterized by a few break frequencies and overall flux normalization. Physical model parameters such as the jet energy and opening angle, the microphysical shock parameters, and the density and density profile of the circumburst medium may be determined by capturing the full synchrotron spectral energy distribution (SED) and its temporal evolution, which typically requires observations spanning the full electromagnetic spectrum.

Despite the success of this basic picture, increasingly detailed observational campaigns of GRBs over the past decade have demonstrated the need to incorporate additional physics. One of the most important additions has been the detection of reverse shock (RS) emission, a second synchrotron component from a second shockwave propagating back into the jet (Laskar et al. 2013; Perley et al. 2014; van der Horst et al. 2014). The RS emission reveals details of the jet's magnetization and initial bulk Lorentz factor (Sari & Piran 1999; Kobayashi & Zhang 2003; Zhang & Kobayashi 2005). Additional model extensions, from the inclusion of multiple ejecta shells moving at different Lorentz factors (Rees & Meszaros 1998; Jóhannesson et al. 2006; Laskar et al. 2015) to the consideration of emission from electrons not accelerated in the FS (thermal electrons; Eichler & Waxman 2005; Ressler & Laskar 2017; Warren et al. 2018; Margalit & Quataert 2021), have also been explored in the literature. Further extensions may be needed to elucidate several aspects of GRB observations that remain unexplained. These include the detection of very-high-energy photons (VHE; >1 TeV) associated with some GRBs (Abdalla et al. 2019; MAGIC Collab 2019; Blanch et al. 2020; H. E. S. S. Collaboration et al. 2021) and unusual radio evolution inconsistent with variability due to extrinsic scattering from the interstellar medium (ISM) or the standard synchrotron emission framework (Frail et al. 2004; Bright et al. 2019; Kangas & Fruchter 2021; Levine et al. 2023). Numerical simulations may provide the ultimate solution to these oddities, but rely on uncertain assumptions about particle acceleration physics, magnetic field structure, etc.

On 2022 October 9, the Fermi Gamma-Ray Burst Monitor (GBM) and the Swift Burst Alert Telescope (BAT) triggered on a new γ-ray source, rapidly confirmed to be the brightest GRB ever seen by these instruments and designated GRB 221009A

(Dichiara et al. 2022; Veres et al. 2022; Williams et al. 2023). These detections were followed by numerous others across the electromagnetic spectrum, confirming a bright optical, X-ray, and radio counterpart (Kennea et al. 2022b; Dichiara et al. 2022; Lipunov et al. 2022; Bright et al. 2022) and a redshift of 0.151 (de Ugarte Postigo et al. 2022a; Malesani et al. 2023). GRB 221009A also exhibited coincident VHE emission, with photons reported up to 18 TeV (Huang et al. 2022) and potentially as high as 250 TeV (Dzhappuev et al. 2022). Although a calculation of the isotropic-equivalent energy released in γ-rays for this burst is complicated by saturation effects at multiple γ-ray instruments, preliminary estimates yield $\log E_{\gamma,\mathrm{iso}} \approx 54.77$ (0.1 keV–100 MeV), one of the highest values to date (Kann & Agui Fernandez 2022).

Several groups have modeled the afterglow emission from GRB 221009A (Ren et al. 2022; Sato et al. 2022; Fulton et al. 2023; Guarini et al. 2023). Fulton et al. (2023) focus solely on the optical and X-ray afterglow in the context of characterizing a possible emerging supernova (SN) component at ~20 days. The other three groups use radio, optical, X-ray, and/or γ-ray observations taken at $\lesssim 12$ days post-discovery[32] (Ren et al. 2022; Sato et al. 2022; Guarini et al. 2023). Although the details of each model differ, common findings among the three groups include a high isotropic-equivalent kinetic energy and a high degree of collimation for the jet and a low-density environment. In all analyses, the best-fit model cannot explain all of the data, suggesting that GRB 221009A may be an ideal test case for more complex models incorporating more realistic physics.

Here, we present detailed radio, millimeter, optical, X-ray, and γ-ray observations of GRB 221009A, spanning 15 orders of magnitude in frequency and four orders of magnitude in time (extending to ~100 days). We find that a standard synchrotron FS model can explain large portions of the data, revealing that GRB 221009A's extraordinary brightness is due to the jet's unusual degree of collimation, rather than an intrinsically large energy. However, the model struggles to reproduce some aspects of the full data set, in particular the radio and millimeter emission. We show that standard extensions to the synchrotron FS model (e.g., the addition of a RS) are unsuccessful at explaining our observations, suggesting that at least one of the basic assumptions underlying our standard picture of GRB afterglow emission needs to be revisited.

Unless otherwise noted, all times refer to times after the GBM trigger (2022 October 9 13:16:59.000 UTC; Veres et al. 2022), and all magnitudes are in the AB system, not corrected for Galactic or intrinsic dust extinction. We employ Lambda cold dark matter (ΛCDM) cosmological parameters of $\Omega_m = 0.31$, $\Omega_\Lambda = 0.69$, and $H_0 = 68$ km s^{-1} Mpc^{-1} throughout, and assume a Galactic extinction of $A_V = 4.1034$ mag (Schlafly & Finkbeiner 2011). The redshift of $z = 0.151$ corresponds to a luminosity distance of $D_L = 2.28 \times 10^{27}$ cm for this burst.

2. Observations and Data Analysis

2.1. Radio

2.1.1. Giant Metrewave Radio Telescope

We observed the afterglow using the upgraded Giant Metrewave Radio Telescope (GMRT) through program 43_039 (PI: Laskar) starting 18.0 days, 21.9 days, and 21.8 days after the

---

[32] Based on information available at the time of submission of this manuscript.

Table 1
Radio Observations of GRB 221009A

Telescope	Frequency[a] (GHz)	Time[b] (days)	Flux Density (mJy)	Uncertainty (μJy)
MeerKAT	1.28	1.26	2.10	24
ALMA	97.5	2.36	9.21	90
SMA	231	2.68	9.44	900
...	...	...	...	...

Notes.
[a] Central frequency.
[b] Mid-time since Fermi/GBM trigger. The full data table is available as an enhanced machine-readable table online.

(This table is available in its entirety in machine-readable form.)

burst in bands 3 (400 MHz), 4 (750 MHz), and 5 (1260 MHz), respectively. The observations utilized 400 MHz bandwidth. We used J1925+2106 for complex gain calibration, and either 3C 286 or 3C 48 for bandpass and flux-density calibration, depending on availability. For Band 3, we carried out data reduction via standard techniques using the Common Astronomy Software Applications (CASA; McMullin et al. 2007), including three rounds of phase self-calibration, followed by two rounds of amplitude and phase self-calibration. For Band 4 and Band 5, we reduced and imaged the data using the capture pipeline (Kale & Ishwara-Chandra 2021). We list the results of our uGMRT observations in Table 1.

2.1.2. MeerKAT

We observed the afterglow with the MeerKAT radio telescope beginning at ≈1.3 days after the burst in the *L* band (1.3 GHz) via program SCI-20220822-TL-01 (PI: Laskar). Later observations employed simultaneous subarray-mode observations in the *L* and *UHF* bands. The observations employed 1938-634 as the bandpass and flux-density calibrator, and J1925+2106 as the complex gain calibrator. The pipeline SDP images were of sufficient quality for photometry of the afterglow using CASA. The noise in the image of *L*-band data taken on 2022 October 15 was much higher than in the other epochs due to significant radio frequency interference contamination. We report our MeerKAT photometry in Table 1.

2.1.3. Very Large Array

We obtained seven epochs of multifrequency observations of GRB 221009A beginning ≈3.5 days after the burst with the Karl G. Jansky Very Large Array (VLA) through program 22B_062 (PI: Laskar). The observations employed either 3C 286 or 3C 48 for bandpass and flux-density calibration and J1925+2106 for complex gain calibration. We imaged the pipeline-calibrated measurement sets downloaded from the VLA archive, where available. For the second epoch, taken on 2022 October 15, the flux-calibrator scans were defective. We calibrated this observation using flux-calibrator data at the same frequencies taken from the first epoch, instead, and achieved excellent agreement for the derived flux density of the gain calibrator. The pattern of the imaging residuals in the second and third epochs indicated gain errors, which we ameliorated via phase and amplitude self-calibration using an automated self-calibration pipeline.[33] We report the results of our VLA observations in Table 1.

2.1.4. Very Long Baseline Array

We obtained four epochs of observations of GRB 221009A with the Very Long Baseline Array (VLBA) and the 100 m radio telescope Effelsberg at 8.3 GHz, beginning ≈12.4 days after the burst, under project VLBA/22B-305 (Legacy Code BL073; PI: Laskar). The full-track observations utilized 3C 345 and 3C 454.3 as fringe calibrators and were phase referenced to TXS 1903+196 (JVAS J1905+1943), a compact quasar at $z = 2.3$, with cycles of 168 s on target and 68 s on the calibrator. We carried out standard fringe fitting,[34] bandpass, and complex gain calibration using AIPS (Greisen 2003). We interpolated the delay and rate solutions to GRB 221009A and produced phase-reference images. We measured the flux density using JMFIT in AIPS in the image plane and with MODELFIT in DIFMAP (Shepherd et al. 1994) in the *uv* plane, obtaining similar results within a few percent. We corrected the derived flux densities for the primary beam for the first epoch and rescaled according to the calibrator flux in the fourth epoch. We present the inferred total (CLEANed) flux-density measurements from our VLBA observations in Table 1.

2.1.5. Australia Telescope Compact Array

We obtained four epochs of observations of the afterglow with the Australia Telescope Compact Array (ATCA) beginning ≈5.8 days after the burst by triggering our program C3289 (PI: Laskar) using the CABB correlator tuned to 15 mm (with 2 GHz basebands tuned to 16.7 and 21.2 GHz) and 7 mm (33 and 35 GHz, and also 45 and 47 GHz). The observations were carried out by the observatory in service mode under project CX515, and employed PKS1921-293 for bandpass calibration, PKS1934-638 for flux-density calibration, and PKS1923+210 (J1925+2106) for complex gain calibration. We calibrated the data using MIRIAD (Sault et al. 1995), and combined the 33 GHz and 35 GHz data, as well as the 45 GHz and 47 GHz data, prior to imaging in CASA. The cleaning process reveals residuals characteristic of phase decorrelation and the resulting ATCA SEDs are extremely steep and are inconsistent with an extrapolation to nearly contemporaneous Atacama Large Millimeter/submillimeter Array (ALMA) observations. Whereas phase-only self-calibration recovers some flux, the signal-to-noise ratio (S/N) in the data is too low for adequate self-calibration. We list the ATCA measurements in Table 1 for completeness, but we do not use these in our subsequent modeling, and we caution against the use of these data in other works without more careful attention to the calibration.

2.1.6. Atacama Large Millimeter/submillimeter Array

We obtained seven epochs of ALMA Band 3 (3 mm) observations of GRB 221009A beginning ≈2.4 days after the burst through program 2022.1.01433.T (PI: Laskar). The observations utilized two 4 GHz wide basebands centered at 91.5 and 103.5 GHz, respectively. The first five epochs used J1924-2914 as flux-density calibrator. The sixth epoch used J1550+0527; this execution was affected by a correlator issue and was reobserved, this time using J2232+1143. The seventh epoch used J1550+0527. All epochs used J1914+1636 as complex gain calibrator. Our ALMA coverage has a gap

---

[33] https://github.com/jjtobin/auto_selfcal

[34] To account for the structure of the complex gain calibrator, we derived a clean-component model by first imaging the data after a preliminary fringe fit and used this model for subsequent calibrations.

between ≈15 and 75 days due to the shutdown of the observatory following a cyber attack. We downloaded the pipeline-generated images from the ALMA archive and performed photometry in CASA. We report our photometry in Table 1.

2.1.7. Northern Extended Millimeter Array

We obtained two epochs of Northern Extended Millimeter Array (NOEMA) 97.5 GHz observations of GRB 221009A at 39.2 and 54.2 days after the burst through program S22BE (PI: Laskar). The observations utilized two 7.7 GHz wide base-bands centered at 89.8 and 105.2 GHz, respectively. We used MWC349 as flux-density calibrator, B2200+420 (epoch 1) and 3C 454.3 (epoch 2) as bandpass calibrators, and 1932+204 and 1923+210 as complex gain calibrators. Data were reduced in GILDAS[35] using standard procedures by observatory staff and provided to us. We imaged the reduced data in CASA and report our photometry in Table 1.

2.1.8. Submillimeter Array

We observed the afterglow with the Submillimeter Array (SMA) at a combination of 1.3 mm (≈230 GHz) and 1.1 mm (290 GHz) for seven epochs using Uranus as flux-density calibrator, 3C 84 as bandpass calibrator, and interleaved observations of J1925+211 and MWC349a for complex gain calibration. We calibrated the data in Millimeter Interferometer Reduction[36] (MIR; the in-house calibration suite for the SMA) and measured the afterglow flux density using vector averaging of the uv data (verified by imaging of the first two epochs). An additional 850 μm observation yielded an upper limit. We report the results of our SMA observations in Table 1.

2.2. Optical

We observed GRB 221009A in *griz* filters with IO:O on the Liverpool Telescope (LT; Steele et al. 2004) at multiple epochs beginning on 2022 October 9. We downloaded pipeline-reduced images from the LT archive. To avoid contamination from nearby sources in the crowded field, we use a custom script to construct a model of the point-spread function and subtract the wings of several bright stars after masking the inner pixels, as needed. We report aperture photometry performed in a 1″.0 radius aperture calibrated to the Pan-STARRS1 catalog in Table 2. We additionally include optical and near-infrared (NIR) data reported in GCN circulars, from Xu et al. (2022), Brivio et al. (2022), Rastinejad & Fong (2022), O'Connor et al. (2022a), D'Avanzo et al. (2022), Huber et al. (2022), Ferro et al. (2022), and O'Connor et al. (2022b), and radio observations from de Ugarte Postigo et al. (2022b) and Leung et al. (2022) in our analysis. We do not include Hubble Space Telescope (HST) observations from Levan et al. (2022) in our work as the corresponding photometry likely contains contamination from an underlying host galaxy, and require deep, late-time templates for subtraction.

Table 2
Liverpool Telescope Observations of GRB 221009A

Δt [a] (days)	Filter	Mag (AB)	Uncertainty	t_{int} (s)	Seeing (arcsec)
0.33486	g	18.57	0.04	45	1.17
0.33749	z	15.29	0.01	45	1.04
0.33662	i	15.96	0.01	45	1.08
0.33576	r	16.99	0.01	45	1.40
0.34899	g	18.53	0.04	50	1.01
0.34987	r	17.05	0.01	40	0.99
0.35061	i	16.00	0.01	30	0.90
0.35132	z	15.33	0.01	30	0.89
0.39745	g	18.55	0.05	50	1.36
0.39978	z	15.48	0.01	30	1.02
0.39834	r	17.21	0.01	40	1.01
0.39908	i	16.15	0.01	30	0.96
1.27230	r	18.85	0.02	45	0.87
1.27097	g	20.33	0.06	100	1.34
1.27404	z	17.06	0.01	45	1.03
1.27316	i	17.77	0.01	45	0.84
1.30908	r	18.87	0.02	90	1.08
1.31046	i	17.80	0.01	90	1.03
1.31186	z	17.10	0.01	90	1.00
1.39474	g	20.41	0.12	100	1.17
1.39607	r	19.03	0.04	45	1.06
1.39694	i	17.93	0.01	45	1.41
1.39781	z	17.21	0.01	45	1.14
2.26839	i	18.69	0.02	100	1.11
2.26689	r	19.84	0.05	100	1.35
2.26991	z	18.02	0.01	100	1.02
2.29593	r	19.84	0.05	60	1.04
2.29441	g	21.05	0.12	120	1.33
2.29698	i	18.73	0.02	60	1.24
2.29803	z	17.99	0.02	60	1.24
3.27665	i	19.29	0.03	120	1.51
3.27434	r	20.31	0.05	180	1.58
3.27863	z	18.43	0.07	120	2.69
3.28182	g	21.61	0.19	180	2.18
3.28371	r	20.33	0.09	60	1.91
3.28475	i	19.28	0.03	60	1.46
3.28579	z	18.55	0.03	60	1.56
7.27887	r	21.60	0.08	180	0.79
7.28154	i	20.44	0.03	180	0.85
7.28571	z	19.68	0.03	360	0.75
7.28992	i	20.37	0.03	180	0.83
7.29263	r	21.44	0.08	180	0.82
8.27806	i	20.58	0.04	240	1.07
8.27470	r	21.68	0.08	240	1.07
8.28328	z	19.94	0.04	480	1.20
8.28854	i	20.69	0.05	240	1.08
8.29195	r	21.91	0.13	240	1.09
10.28995	r	22.04	0.11	300	0.90
10.29366	i	21.07	0.06	240	0.84
10.29887	z	20.27	0.05	480	1.04
10.30412	i	20.92	0.05	240	0.85
10.30788	r	22.04	0.10	300	0.86
11.27403	r	22.09	0.11	360	0.83
11.28344	z	20.50	0.05	480	0.80
11.27821	i	21.12	0.05	240	0.83
11.28871	i	21.17	0.06	240	0.91
11.29292	r	22.09	0.10	360	0.91
14.28998	r	22.45	0.17	360	0.90
14.29496	i	21.47	0.07	360	0.87
14.30262	z	20.83	0.06	720	0.79
14.31111	i	21.35	0.09	240	0.95
14.31535	r	22.35	0.15	360	0.99
17.31003	z	21.08	0.15	720	1.67
18.29124	i	21.91	0.13	720	1.37

Table 2
(Continued)

Δt [a] (days)	Filter	Mag (AB)	Uncertainty	t_{int} (s)	Seeing (arcsec)
18.30665	r	22.99	0.24	1350	1.46
19.27566	z	21.19	0.73	600	1.08
20.27930	z	21.55	0.14	1350	1.23
21.28883	z	21.31	0.12	1350	1.23
36.28571	i	22.23	0.11	1620	1.10
38.27709	r	24.06	0.32	1800	0.87

Note.

[a] Mid-time since Fermi/GBM trigger. The data have not been corrected for extinction in the Milky Way or GRB host galaxy, or for the contribution of host-galaxy light.

(This table is available in machine-readable form.)

2.3. Ultraviolet

We performed photometry in a 5″ aperture on all Swift/ Ultra-violet Optical Telescope (UVOT) images up to and including segment 01126853067 (taken on 2022 December 16) obtained from the Swift repository[37] with the `uvotproduct` (v2.8) software and CALDB version 20221229. This corresponds to almost all of the data taken before the target entered a Sun constraint on 2022 December 21 (lasting until 2023 February 6). We used defaults for all pipeline parameters. We present our UVOT measurements in Table 3 (see also Williams et al. 2023 for an independent analysis of these data). The white-band data is of limited utility owing to the strong foreground extinction and we therefore do not use data in this band for subsequent modeling.

2.4. X-Rays

2.4.1. NuSTAR (3–79 keV)

The Nuclear Spectroscopic Telescope Array (NuSTAR; Harrison et al. 2013) acquired a first set of four observations between 1.96 and 23.73 days (PIs: Margutti & Racusin) with exposure times of ≈20 ks, followed by one deeper exposure at 31.91 days (exposure time of 40 ks; PI: Troja). We reduced the NuSTAR data following standard procedures with the NuSTAR Data Analysis Software (NuSTARDAS) version 0.4.9 and NuSTAR CALDB version 20221130, applying standard filtering criteria with `nupipeline`. GRB 221009A is a bright source of hard X-rays in the NuSTAR bandpass (3–79 keV) at all times. For each epoch we extracted a spectrum with `nuproducts` using a source-extraction region centered at the location of the radio counterpart and different sizes to maximize the S/N, as reported in Table 4. We used a source-free background region of radius >2′. We find that the hard X-ray spectrum is well modeled by a simple power law with a photon index[38] of $\Gamma \approx 1.86$ at all times.

2.4.2. Swift/X-ray Telescope (0.3–10 keV)

The Swift X-ray Telescope (XRT) began observing GRB 221009A ≈3.4 ks after the Swift/BAT trigger and ≈6.6 ks after the Fermi/GBM trigger. We extracted XRT

Table 3
Swift/UVOT Observations of GRB 221009A

Start Time[a] (s)	Stop Time[a] (s)	Band	Mag	Uncertainty
593.2	612.9	*UVB*	17.09	0.13
767.0	786.7	*UVB*	17.21	0.14
1147.9	1332.8	*UVB*	17.50	0.13
40736.7	41644.4	*UVB*	20.21	0.14
56651.5	57558.5	*UVB*	20.72	0.26
337.2	586.9	*UVU*	17.67	0.08
742.1	761.9	*UVU*	17.78	0.25
1122.9	1317.9	*UVU*	17.77	0.18
28831.1	29661.9	*UVU*	20.3	0.21
46079.7	46907.8	*UVU*	20.61	0.27
92151.0	92979.8	*UVU*	20.83	0.31
668.4	688.3	*UVV*	15.56	0.11
841.2	861.0	*UVV*	15.55	0.11
1049.4	1243.1	*UVV*	15.80	0.09
34595.2	35419.7	*UVV*	18.07	0.07
51699.8	52523.8	*UVV*	18.64	0.10
80607.5	81514.3	*UVV*	19.10	0.13
97761.4	98526.1	*UVV*	19.54	0.20

Note.

[a] Since Swift/BAT trigger (add 3199 s to convert to time relative to Fermi/ GBM trigger, and see also Williams et al. 2023). Magnitudes are in the native Swift/UVOT system and have not been corrected for extinction in the Milky Way or GRB host galaxy.

(This table is available in machine-readable form.)

photon counting (PC)-mode spectra at the times corresponding to the NuSTAR epochs using the time-sliced spectrum tool on the Swift website[39] and modeled the spectra, together with corresponding calibration files, in `XSPECv12.12.1`. While the derived photon index appears to increase with time (from ≈1.55 to ≈1.82, tying $N_{H,int}$ across epochs), the evidence for this is marginal ($\lesssim 2\sigma$) and we do not consider this statistically significant (but see also Williams et al. 2023). Tying the photon index across epochs gives results consistent with the parameters on the Swift website.

Finally, we combine the XRT and NuSTAR data together and perform three joint spectral fits: (i) tying both $N_{H,int}$ and Γ_X across epochs; (ii) tying $N_{H,int}$ and allowing Γ_X to vary; and (iii) tying Γ_X and allowing $N_{H,int}$ to vary. We do not find evidence for evolution in Γ_X with time. There is marginal evidence in these fits for a decrease in $N_{H,int}$ from $1.51^{+0.13}_{-0.05} \times 10^{22} \, \text{cm}^{-2}$ to $0.99^{+0.31}_{-0.29} \times 10^{22} \, \text{cm}^{-2}$. However, these numbers are consistent at the 2σ level, and we do not consider varying $N_{H,int}$ further. On tying both quantities across epochs, we find $N_{H,int} = 1.35^{+0.06}_{-0.09} \times 10^{22} \, \text{cm}^{-2}$ and $\Gamma_X = 1.8566^{+0.0033}_{-0.0063}$.

We download the XRT 0.3–10 keV count rate light curve[40] (Evans et al. 2007, 2009) and convert it to flux density at 1 keV for subsequent analysis (after shifting the time to the GBM trigger time) using $\Gamma_X = 1.8566$. For this we use unabsorbed counts-to-flux conversion rates of $1.00 \times 10^{-10} \, \text{erg cm}^{-2} \, \text{ct}^{-1}$ and $1.07 \times 10^{-10} \, \text{erg cm}^{-2} \, \text{ct}^{-1}$ for the windowed timing and PC modes, respectively, obtained from the Swift website. We also extract the NuSTAR flux in the

---

[37] http://www.swift.ac.uk/swift_portal
[38] We define the photon index with the convention $F_E \propto E^{-\Gamma}$.

[39] https://www.swift.ac.uk/xrt_spectra/01126853/
[40] Obtained from the Swift website at http://www.swift.ac.uk/xrt_curves/ 01126853 and rebinned to a minimum S/N per bin of 10.

Table 4
Log of NuSTAR Observations

Start Date/Time (dd-mm-yy/hh:mm:ss)	Stop Date/Time (dd-mm-yy/hh:mm:ss)	Centroid MJD (days)	Time[a] (days)	Net Exposure[b] A (ks)	Net Exposure[c] B (ks)	Source Region Size Radius (')
2022-10-11/10:04:09	2022-10-11/14:45:00	59863.517066	1.96	20.66	20.49	1.5
2022-10-15/05:21:09	2022-10-15/17:16:09	59867.471285	5.92	20.66	20.49	1.1
2022-10-20/01:06:09	2022-10-20/11:56:09	59872.271632	10.72	20.44	20.26	1.0
2022-11-02/06:06:09	2022-11-02/17:01:09	59885.481701	23.73	21.30	21.09	1.0
2022-11-09/23:06:09	2022-11-10/23:01:09	59893.460868	31.91	40.78	40.38	1.0

Notes.
[a] With respect to the Fermi/GBM trigger time.
[b] For NuSTAR module A.
[c] For NuSTAR module B.

(This table is available in machine-readable form.)

Table 5
Fermi/LAT Observations

Start Time[a] (s)	Stop Time[a] (s)	Energy Flux (erg s^{-1} cm^{-2})	Energy Flux Uncertainty (erg s^{-1} cm^{-2})	Photon Flux (ph s^{-1} cm^{-2})	Photon Flux Uncertainty (ph s^{-1} cm^{-2})	Photon Index[b]	Photon Index Uncertainty	Test Statistic
3000.0	4429.2	2.67×10^{-08}	1.43×10^{-08}	3.06×10^{-05}	1.06×10^{-05}	2.10	0.283	57
4429.2	6539.4	9.54×10^{-09}	2.69×10^{-09}	1.12×10^{-05}	1.88×10^{-06}	2.11	0.141	177
9654.9	14254.6	4.44×10^{-09}	1.73×10^{-09}	5.41×10^{-06}	1.37×10^{-06}	2.13	0.209	79
14254.6	21045.8	1.72×10^{-09}	9.79×10^{-10}	2.35×10^{-06}	9.06×10^{-07}	2.19	0.334	30
21045.8	31072.3	1.44×10^{-09}	7.95×10^{-10}	2.01×10^{-06}	8.81×10^{-07}	2.20	0.354	21
31072.3	45875.7	5.70×10^{-10}	2.79×10^{-10}	1.17×10^{-06}	5.26×10^{-07}	2.46	0.402	13
45875.7	67731.6	4.34×10^{-10}	1.80×10^{-10}	1.27×10^{-06}	5.08×10^{-07}	2.87	0.445	12
67731.6	100000.	$<6.42 \times 10^{-10}$	...	$<5.79 \times 10^{-07}$	...	2.00	...	5

Notes.
[a] With respect to the Fermi/GBM trigger time.
[b] Here defined as $F_E \propto E^{-\Gamma}$.

(This table is available in machine-readable form.)

range 15–20 keV and convert it to flux density at 15 keV using the photon index from the joint fit for subsequent analysis.

2.5. γ-Rays: Fermi/Large Area Telescope (100 MeV–100 GeV)

The Large Area Telescope (LAT) instrument on board the Fermi satellite is sensitive to γ-ray photons in the energy band from 30 MeV to 300 GeV (Atwood et al. 2009). We extracted and analyzed the Fermi/LAT data of GRB 221009A using the public software GTBURST, which is distributed as part of the official Fermitools software package.[41] We extracted the LAT data within a temporal window from 3.5 to 100 ks (0.04–1.16 days) after the GBM trigger time. We filtered photons with energies in the 100 MeV–100 GeV range, within a region of interest of 12° centered on the burst position of R.A. $=288°.264$ and decl. $=19°.773$, and with an angle from the spacecraft zenith $<100°$, as part of the standard procedure. We selected the "P8R3 SOURCE" class as the instrument response function, suitable for late-time emission subsequent to the prompt phase of the burst. We extracted light curves assuming a power-law model for the spectrum of the source, together with the "isotropic template" and "template" for the particle background and the Galactic component, respectively. We performed an unbinned likelihood analysis, setting the minimum test statistics to 10 for detections. We calculated flux upper limits

using a photon index of 2 in the energy band of 100 MeV–100 GeV. We report our Fermi/LAT photometry in Table 5.

3. Multiwavelength Modeling

We now interpret the multiwavelength afterglow observations in the context of the standard model of synchrotron radiation produced by a relativistic FS produced by the GRB jet propagating into the pre-explosion environment. The model is parameterized by the shock energy, $E_{K,iso}$, the radial density profile, $\rho \propto r^{-k}$, of the environment, the density normalization (n_0 for $k = 0$, ISM-like; and A_* for $k = 2$, wind-like[42]), the fraction of shock energy in relativistic electrons (ϵ_e) and magnetic fields (ϵ_B), as well as the index (p) of electrons accelerated to a power-law energy distribution. The observed radiation is expected to be characterized by three break frequencies: (i) the self-absorption frequency, ν_a; (ii) the characteristic frequency, ν_m; and (iii) the cooling break, ν_c. Solving for these parameters requires interrogating the observed light curves and SEDs.

3.1. X-Ray and Optical/NIR: Forward Shock

In order to interpolate observations to common times for constructing and plotting SEDs, we fit the observed multiwavelength light curves to a series of broken power-law models.

---

[41] https://fermi.gsfc.nasa.gov/ssc/data/analysis/gtburst.html

[42] $A_* = 1$ corresponds to a mass-loss rate of $\dot{M}_w = 10^{-5} M_\odot$ yr^{-1} for a wind velocity of $v_w = 10^3$ km s^{-1}.
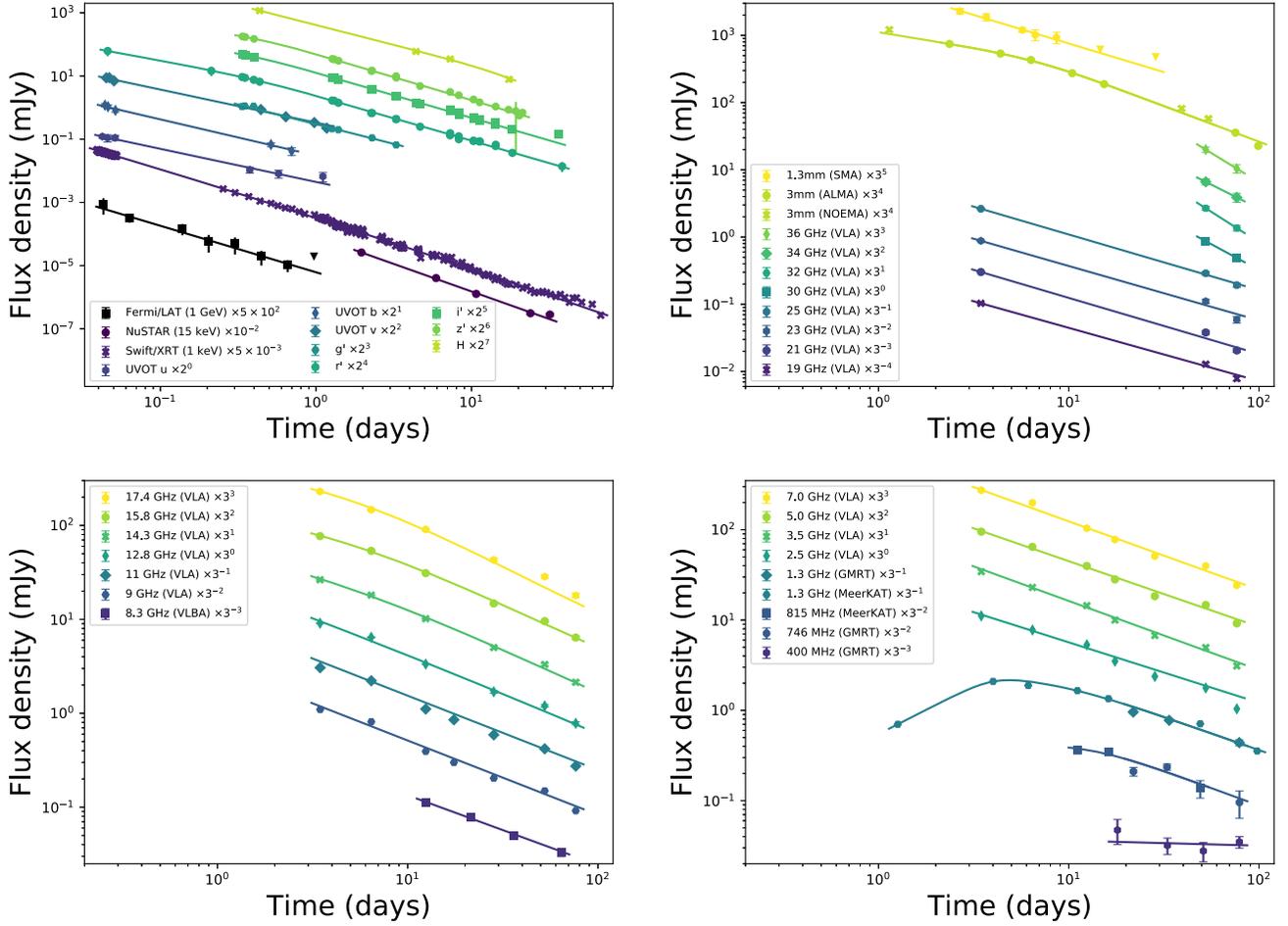
Figure 1. Light curves of GRB 221009A from 1 GeV to 400 MHz together with the broken power-law model fits used to interpolate data to a common time and to inform the multiwavelength modeling (Sections 3.1 and 3.2). The light curves have been multiplied by the factors listed in the legends to offset them in the plot for clarity. The three panels with radio data are on the same temporal scale to facilitate comparison.

The resulting fits are presented in Figure 1. The Fermi/LAT 1 GeV and NuSTAR 15 keV light curves can be fit with a single power law with decay indices,[43] $\alpha_{\mathrm{LAT}} = -1.47 \pm 0.08$ and $\alpha_{15\,\mathrm{keV}} = 1.74 \pm 0.03$. The Swift/XRT 1 keV light curve can be fit with a broken power law with decay indices, $\alpha_{\mathrm{X},1} = -1.46 \pm 0.02$ and $\alpha_{\mathrm{X},2} = -1.70 \pm 0.03$; however, the break time, $t_{\mathrm{b,X}} = (1.0 \pm 0.8)$ day, is not well constrained. The r'-band light curve can be fit with a broken power law with decay indices, $\alpha_{\mathrm{r},1} = -0.92 \pm 0.10$ and $\alpha_{\mathrm{r},2} = -1.42 \pm 0.01$ and break time, $t_{\mathrm{b,r}} = (0.40 \pm 0.04)$ day, although the pre-break decay is contingent upon uncertain photometry reported in GCN circulars. Correcting the r'-band flux for Milky Way extinction, the NIR-to-optical spectral index at ≈ 4.4 days is $\beta_{\mathrm{NIR-opt}} = -0.76 \pm 0.04$, while the NIR-to-X-ray spectral index is similar, $\beta_{\mathrm{NIR-X}} = -0.70 \pm 0.01$. Spectral indices involving NIR/optical bands are subject to additional, indeterminate systematic errors due to unknown uncertainties on the Galactic extinction along the line of sight and any additional intrinsic extinction.

A shallower light curve in the optical compared to the X-ray usually indicates[44] an ISM-like environment with $\nu_{\mathrm{opt}} < \nu_{\mathrm{c}} < \nu_{\mathrm{X}}$. However, a uniform-density environment is ruled out for this burst by the closure relations between the light-curve decay rates and spectral indices. To see this, we start with the optical spectral index of $\beta_{\mathrm{NIR-opt}} \approx -0.76$, which requires an electron energy index of $p \approx 2.52$ in the regime $\nu_{\mathrm{opt}} < \nu_{\mathrm{c}} < \nu_{\mathrm{X}}$. This would imply $\alpha_{\mathrm{X}} = (2-3p)/4 \approx -1.4$, which is shallower than observed. Furthermore, the similarity between $\beta_{\mathrm{NIR-opt}}$ and $\beta_{\mathrm{NIR-X}}$ suggests that no spectral break is present between these bands. If we instead consider the regime $\nu_{\mathrm{opt}} < \nu_{\mathrm{X}} < \nu_{\mathrm{c}}$, and $p \approx 2.52$ from the spectral indices, then the predicted light-curve decline rates of $\alpha_{\mathrm{opt}} \approx \alpha_{\mathrm{X}} \approx -1.1$ are significantly shallower than observed in either band. Finally, in the regime $\nu_{\mathrm{c}} < \nu_{\mathrm{opt}} < \nu_{\mathrm{X}}$, the observed spectral indices would indicate $p \approx 1.5$, which predicts a light-curve decline rate of $\alpha = -(3p + 10)/16 \approx -0.9$ (Dai & Cheng 2001; Zhang & Mészáros 2004), again much shallower than observed in either band. While this can be remedied by interposing a jet break (after which the light curve declines at $\approx -p$, including exponential sideways spreading; Rhoads 1999; Sari et al. 1999) at $t_{\mathrm{jet}} \approx 1$ day, in this model the jet quickly becomes nonrelativistic and the resulting evolution cannot match the radio observations (Section 3.2). We note that Sato et al. (2022) came to a similar conclusion even without radio data but incorporating Fermi/LAT GeV observations. For completeness, we present an ISM model, together with its shortcomings, in Appendix A.

---

[43] We use the convention $F_\nu \propto t^\alpha \nu^\beta$ throughout.

[44] Whereas the presence of a SN could also make optical light curves shallower, as we discuss later in this section, we find no strong additional evidence for such a component.
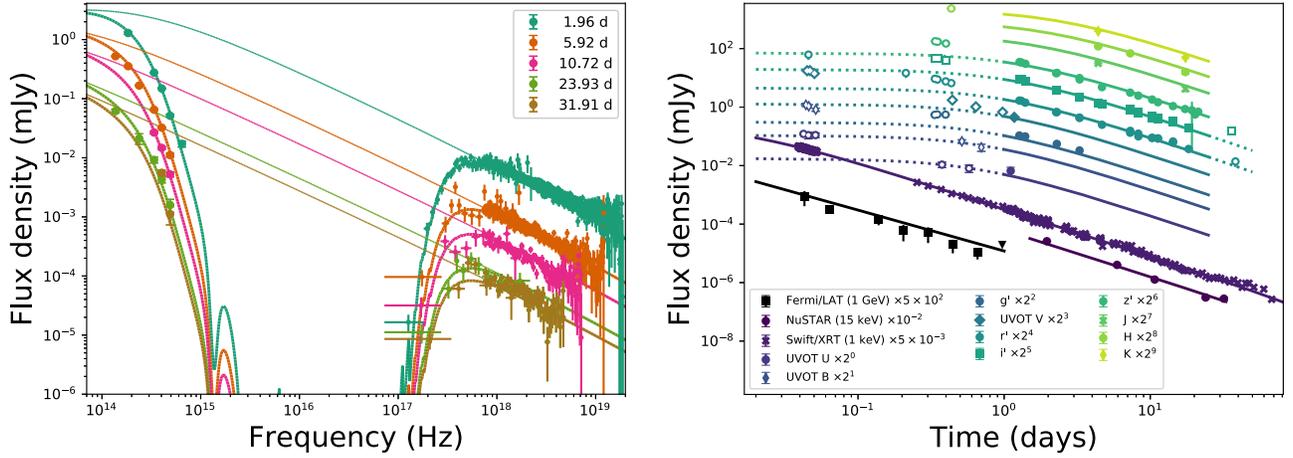
Figure 2. SEDs (left) and a sampling of available light curves (right) at X-ray, UV, optical, and NIR wavelengths of GRB 221009A (data points), together with the highest-likelihood FS wind model (lines) that explains most of these observations (Section 3.1). Thin lines indicate the underlying synchrotron spectrum. The break at $\approx 2 \times 10^{14}$ Hz in the first epoch is ν_{m}. The X-ray SEDs shown here are the result of joint spectral fits of Swift and NuSTAR observations at the corresponding times (Section 2.4.2). Optical points have been interpolated using the best-fit broken power-law light curves (Figure 1). The model cannot explain the UV/optical light curves at $\lesssim 1$ day; these points (open symbols) were excluded from the fit. These caveats are discussed further in Section 4.3.

We next consider the other standard case of $k = 2$ for the density profile of the pre-explosion environment. The $\nu_{\mathrm{c}} < \nu_{\mathrm{opt}} < \nu_{\mathrm{X}}$ regime is ruled out as in the ISM case, as in this regime the light curves are agnostic to the density profile. In the regime $\nu_{\mathrm{opt}} < \nu_{\mathrm{c}} < \nu_{\mathrm{X}}$, the optical spectral index again requires $p \approx 2.52$. The predicted light-curve decay rates are $\alpha_{\mathrm{opt}} \approx -1.64$ and $\alpha_{\mathrm{X}} \approx -1.39$; however, the opposite is observed.[45] In addition, in this regime we expect an X-ray spectral index of $\beta_{\mathrm{X}} = -p/2 \approx -1.26$, which is significantly steeper than the observed. Finally, we consider the regime $\nu_{\mathrm{opt}} < \nu_{\mathrm{X}} < \nu_{\mathrm{c}}$. The spectral index between the Swift/XRT band at 1 keV and the Fermi/LAT band at 1 GeV is $\beta_{\mathrm{keV-GeV}} = -1.10 \pm 0.04$. This is significantly steeper than the X-ray spectral index alone. Furthermore, the spectral index in the GeV band of $\beta_{\mathrm{GeV}} = 1 - \Gamma_{\mathrm{GeV}} \approx -1.2$ (using a weighted-mean photon index; see Table 5) also appears steeper than the X-ray data alone, supporting the presence of a spectral break between the X-ray and GeV bands. While the optical and X-ray spectral indices and decay rates ought to be equal to each other in this regime, a potential solution[46] for the shallower optical decay observed could be the proximity of ν_{m} to the optical/NIR bands.

We find that we are able to find a relatively satisfactory solution with $k = 2$ for $p \approx 2.5$ in the regime $\nu_{\mathrm{m}} \lesssim \nu_{\mathrm{opt}} < \nu_{\mathrm{X}} < \nu_{\mathrm{c}} < \nu_{\mathrm{LAT}}$ (Figure 2) with the following caveats: (i) this model does not match any of the radio observations (although this is also true for the ISM model; see Appendix A), and overpredicts the ALMA 97.5 GHz data point at ≈ 100 days; (ii) the model overpredicts the NIR (*JHK*) flux at the $\approx 30\%$ level; and (iii) in the optical, this model underpredicts the observed light curves at both $\lesssim 1$ day and $\gtrsim 30$ days. We discuss point (i) in Section 3.2 and points (ii) and (iii) in Section 4.3.

To explore this FS model further, we fit the Fermi/LAT light curve at 1 GeV, the Swift/XRT light curve at 1 keV, the UV/

optical/NIR data at 1–30 days, and the 97.5 GHz data point at ≈ 100 days simultaneously by sampling the parameter space of p, $E_{\mathrm{K,iso}}$, A_*, ϵ_{e}, ϵ_{B}, and t_{jet} using Markov Chain Monte Carlo (MCMC) sampling with emcee (Foreman-Mackey et al. 2013). The details of our implementation are described in Laskar et al. (2013, 2014). We run 512 walkers for 5000 steps and discard the first 100 steps as burn-in. We use a uniform prior on p from 2.001 to 2.99. We restrict $\log(\epsilon_{\mathrm{e}})$ and $\log(\epsilon_{\mathrm{B}})$ to the range $\in (-5, 0)$ and require $\epsilon_{\mathrm{e}} + \epsilon_{\mathrm{B}} < 1$. We constrain $\log(A_*) \in (-10, 10)$, $E_{\mathrm{K,iso}}/\mathrm{erg} \in (10^{48}, 5 \times 10^{58})$, and $\log(t_{\mathrm{jet}}/\mathrm{days}) \in (-5, 5)$ and use Jeffreys (1946) priors for these last five parameters. To account for systematic flux-calibration offsets in any given band in our data set as well as to prevent single, high-S/N points from driving the entire fit, we implement a minimum uncertainty floor of 10% prior to running the fit. We fix the Galactic extinction to $A_{\mathrm{V,gal}} = 4.1$ mag, and find some evidence for additional extinction, $A_{\mathrm{V,host}} \approx 0.2$ mag. However, we note that there is a degeneracy between $A_{\mathrm{V,gal}}$ and $A_{\mathrm{V,host}}$ as the redshift is low; thus, it is entirely possible that the true Galactic extinction is lower and the true extinction along the line of sight through the host galaxy is higher than the inferred value.

In the highest-likelihood model, the synchrotron break frequencies are located at $\nu_{\mathrm{a}} \approx 2 \times 10^5$ Hz, $\nu_{\mathrm{m}} \approx 4.5 \times 10^{14}$ Hz, and $\nu_{\mathrm{c}} \approx 3.8 \times 10^{19}$ Hz at 1 day, with $\nu_{\mathrm{m}} \approx \nu_{\mathrm{opt}} < \nu_{\mathrm{X}} < \nu_{\mathrm{c}} < \nu_{\mathrm{LAT}}$, as expected. The proximity of ν_{m} to the optical contributes to a shallower optical light curve than expected for the regime $\nu_{\mathrm{m}} < \nu_{\mathrm{opt}} < \nu_{\mathrm{c}}$. The proximity of ν_{c} to the X-rays results in a spectral index intermediate between $\beta = (1 - p)/2 \approx -0.76$ and $\beta = -p/2 \approx -1.3$. The resulting SED fits the NuSTAR spectra well, even though those data were not included in the fit. Finally, the spectral index of $\beta = -p/2 \approx -1.3$ closely corresponds to the value of $\beta_{\mathrm{GeV}} \approx -1.2$ in the Fermi/LAT band at 1 GeV. The proximity of ν_{c} to the X-rays contributes to curvature in the Swift/XRT light curve, and this curvature is sufficient to explain the "break" inferred from a broken power-law fit to the data at 1 keV (Figure 1). Thus, a jet break at ≈ 1 day (D'Avanzo et al. 2022) is not required by the data under this model.

We summarize the results of our MCMC analysis in Table 6. The electron index p is sharply constrained by the X-ray light

---

[45] This remains a fundamental issue in modeling this burst, as we discuss in Section 4.3.

[46] Fulton et al. (2023) assume the same spectral regime of $\nu_{\mathrm{opt}} < \nu_{\mathrm{X}} < \nu_{\mathrm{c}}$ and instead explain the shallower optical light curve compared to the X-rays as contribution from an underlying SN in the optical. However, they also require strongly time-varying extinction for this scenario to explain the observed optical color.

Table 6
Forward-shock Model Parameters

Parameter	Best Fit	MCMC[a]
p	2.531	2.53 ± 0.01
$\log \epsilon_{\mathrm{e}}$	-0.616	$-0.56^{+0.08}_{-0.07}$
$\log \epsilon_{\mathrm{B}}$	-0.221	$-0.40^{+0.20}_{-0.26}$
$\log A_*$	-3.612	$-3.50^{+0.16}_{-0.13}$
$\log(E_{\mathrm{K,iso}}/\mathrm{erg})$	54.04	53.99 ± 0.07
$\log(t_{\mathrm{jet}}/\mathrm{d})$	2.110	$2.14^{+0.16}_{-0.11}$
θ_{jet}	1.46	$1.64^{+0.28}_{-0.20}$
$A_{\mathrm{V,host}}$	0.24	0.23 ± 0.02
$\log(E_{\mathrm{K}}/\mathrm{erg})$	50.55	$50.60^{+0.09}_{-0.07}$
$\log(\nu_{\mathrm{a,f}}/\mathrm{Hz})$[b]	5.3	…
$\log(\nu_{\mathrm{m,f}}/\mathrm{Hz})$	14.6	…
$\log \nu_{\mathrm{c,f}}/\mathrm{Hz})$	19.6	…
$\log(F_{\nu,\mathrm{m,f}}/\mathrm{mJy})$	0.98	…

Notes. Frequencies and flux densities are calculated at 1 day.
[a] Summary statistics from the marginalized posterior density distributions, with median and $\pm 34.1\%$ quantiles (corresponding to $\pm 1\sigma$ for Gaussian distributions; see Figure 3).
[b] This frequency is not directly constrained by the data.

curve, the NIR-to-X-ray spectral index, and the X-ray-to-GeV spectral index. As ν_{a} is unconstrained in this model, the physical parameters ($E_{\mathrm{K,iso}}$, A_*, ϵ_{e}, ϵ_{B}) exhibit degeneracies (Figure 3). The observed 3 mm flux at ≈100 days is lower than expected from a spherical FS, and this drives a jet break[47] at around this time in the model, yielding a small jet opening angle,[48] $\theta_{\mathrm{jet}} \lesssim 2°$.

As mentioned earlier, this model (i) somewhat (≈30%) overpredicts the NIR (JHK) flux (Figure 2), and (ii) underpredicts the optical emission at $\lesssim 1$ day and at $\gtrsim 30$ days. We speculate that the mismatch in the NIR may be related to the inability of this model to also fit the radio data, as discussed next in Section 3.2. We discuss these discrepancies in the NIR and optical, together with additional caveats on the FS modeling, in Section 4.3.

We note that our model parameters are somewhat different from the analyses of Ren et al. (2022) and Sato et al. (2022; notably, we find a much higher value of ϵ_{B}. However, these papers rely solely on data collected within $\lesssim 7$ and $\lesssim 12$ days of GRB 221009A's discovery, respectively. When compared to our more extensive data set, we find that both previously proposed models dramatically overpredict the radio emission at $t \gtrsim 5$ days and are therefore ruled out. Finally, in contrast to Fulton et al. (2023), we do not include a SN contribution to our model, as this does not appear to be required by the data. In particular, there is no strong evidence for excess emission relative to the afterglow model in any of the optical or NIR light curves. This suggests that the contribution of the SN is lower than the flux level of the observed multifrequency optical/NIR light curves. Further investigation of the SN

requires spectroscopic information, and we defer a detailed discussion of the SN to papers focused on this emission component. We also do not include host-galaxy emission in our model. While host emission is known to affect the HST data (not included here) at ≈30 days (Levan et al. 2022), we do not expect the host galaxy to make a significant contribution in the optical light curves at the earlier times ($\lesssim 20$ days) considered here.

3.2. Radio: Multiple Components

In Figure 4, we present our VLA SEDs together with data from GMRT, ALMA, and NOEMA at 400 MHz, 800 MHz, 1.3 GHz, 97.5 GHz, and 225 GHz interpolated[49] to the times of the VLA SEDs using their corresponding best-fit broken power-law functions (Figure 1). We also extract XRT SEDs at the times of the VLA SEDs and fit for the spectral normalization with spectral parameters fixed from the NuSTAR–XRT joint fit (Section 2.4.2).

We find that the FS model discussed in Section 3.1 underpredicts all the radio observations, except at the highest frequencies (at 97.5 GHz, from ALMA) at $\gtrsim 75$ days. The radio emission is strongly self-absorbed below ≈2 GHz for most of the period spanning ≈3–76 days, while the optically thin spectrum above the radio peak does not match the inverted $\nu^{1/3}$ spectrum expected from the low-energy tail of the minimum-energy electrons. In addition, the spectral index above the peak ($\beta \approx -0.2$) is significantly shallower than $\beta_{\mathrm{NIR-opt}}$ as well as β_{X}. This indicates that either the radio emission arises from a separate emission component or the approximation of the electron power law being truncated at a minimum Lorentz factor ($\gamma_{\min}$) breaks down in this case.

Fitting the radio SEDs at $\lesssim 50$ GHz with fiducial, broken power-law models of the form

$$F_\nu = F_{\mathrm{peak}} \left[\frac{1}{2}\left(\frac{\nu}{\nu_{\mathrm{peak}}}\right)^{-s\beta_1} + \frac{1}{2}\left(\frac{\nu}{\nu_{\mathrm{peak}}}\right)^{-s\beta_2} \right]^{-1/s}, \quad (1)$$

separately in each epoch, we find evidence for a slowly decreasing peak flux ($f_{\nu,\mathrm{peak}} \propto t^{-0.70\pm0.02}$) and peak frequency ($\nu_{\mathrm{peak}} \propto t^{-0.49\pm0.02}$) with time (Figure 5 and Table 7). From these fits, we confirm that the spectral index above the peak is shallow, $\beta_{\mathrm{radio}} \approx -0.2$ at $\lesssim 28$ days, steepening marginally to ≈ -0.4 at ≈52 days, and not well constrained thereafter. An extrapolation of the centimeter-band spectrum to the millimeter band underpredicts the 97.5 GHz flux density by ≈20%–50%. Furthermore, the mean spectral index between the ALMA (3 mm) and SMA (1.3 mm) bands over this period is fairly flat, $\beta_{\mathrm{mm}} = -0.02 \pm 0.13$. Thus, the millimeter-band emission cannot be easily subsumed into this additional radio component without either invoking additional high-frequency structure in the emission or invoking additional sources of systematic uncertainties.

The spectral index between the centimeter-band peak in the first VLA epoch at ≈3.46 days at 2.5 GHz and the ALMA 3 mm (97.5 GHz) observation is $\beta = -0.106 \pm 0.002$, which is shallower than the centimeter-band spectral index alone. We test whether phase decorrelation at $\gtrsim 10$ GHz in the VLA

---

[47] We note that the jet-break time is bounded below by the absence of a steep decline in the X-ray light curve to $t_{\mathrm{jet}} \gtrsim 70$ days.
[48] In some models, the jet break is instead interpreted as a viewing-angle effect (Mészáros et al. 1998; Dai & Gou 2001; Zhang & Mészáros 2002). For a given set of observed light curves, this framework implies a beaming-corrected energy greater than that computed under the standard jet-break interpretation by a factor of $1 + 2\ln(\theta_{\mathrm{jet}}/\theta_c)$, where θ_c is some narrow opening angle within which the outflow energy per unit solid angle is roughly constant (Rossi et al. 2002).

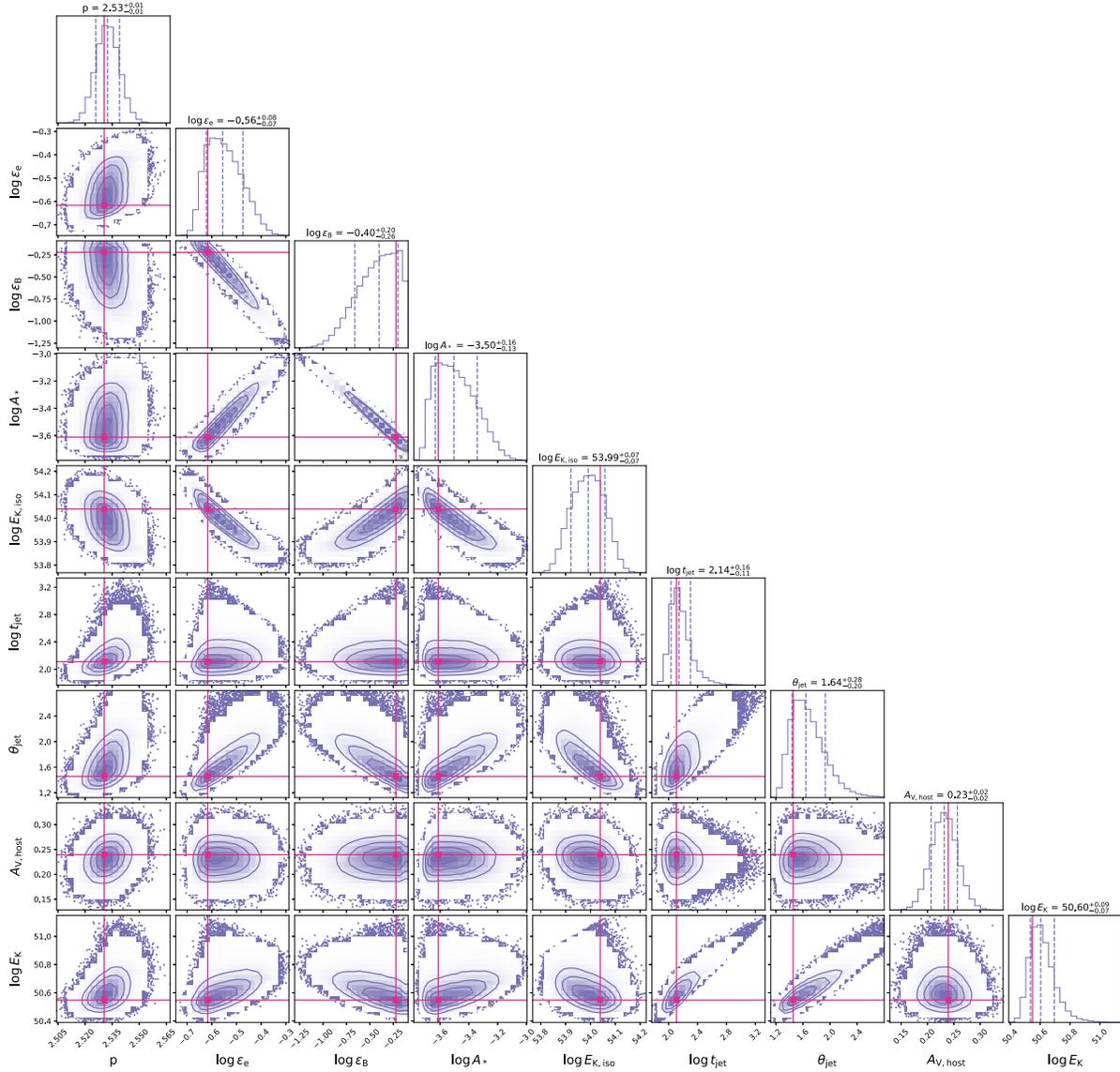[49] The typical temporal dispersion of data points in a given SED is ≈10%.

Figure 3. Correlations and marginalized posterior density from multiwavelength modeling of GRB 221009A with $E_{\mathrm{K,iso}}$ and E_{K} in erg. We compute the opening angle (θ_{jet}) in degrees from $E_{\mathrm{K,iso}}$, A_*, and t_{jet}. The contours enclose 39.3%, 86.4%, and 98.9% of the probability mass in each correlation plot (corresponding to 1σ, 2σ, and 3σ regions for two-dimensional Gaussian distributions), while the dashed lines in the histograms indicate the 15.9%, 50% (median), and 84.1% quantiles (corresponding to $\pm 1\sigma$ for one-dimensional Gaussian distributions). The distribution for ϵ_{B} cuts off at high values due to the prior bound of $\epsilon_{\mathrm{e}} + \epsilon_{\mathrm{B}} < 1$. Strong correlations are evident between most parameters as ν_{a} is unconstrained in this model. See Table 6 for a summary.

observations could be responsible for a loss in observed flux density at higher frequencies by self-calibrating the highest-frequency K-band (25 GHz) observations in the first epoch at ≈ 3.46 days. This process significantly reduces the imaging residuals but only marginally increases the 25 GHz flux density by 4%, whereas making this flux consistent with the $\beta \approx -0.1$ power law would instead require an increase of $\approx 10\%$. We recognize that all radio observations are subject to a systematic flux-density uncertainty of $\approx 10\%$ from the flux-calibration process, which is not incorporated into the analysis above. Thus, if the true centimeter-band flux were systematically higher by this amount at 25 GHz (but not at 2.5 GHz), then there remains a possibility that the centimeter band and millimeter band could yet be ascribable to the same additional component.

We consider the possibility that the entire multifrequency (radio to GeV) afterglow emission may in fact arise from a single emission component, but with nonstandard evolution of break frequencies and fluxes. To test this, we anchor the peak of the SED (in F_ν) as observed in the centimeter band, and evolve it in time according to the inferred peak frequency and peak flux evolution from the broken power-law fits to the radio SEDs (Table 7). We assume spectral indices of $\beta_1 = 2.5$ and $\beta_2 = -0.2$ below and above the peak, respectively. Upon extrapolating this spectrum to the optical, we find that an additional extinction of $A_{\mathrm{V,host}} \approx 0.2$ mag is needed to match the optical flux, although this is still only possible at $\gtrsim 3$ days. A spectral break is needed above the optical in order to not overpredict the X-ray flux. We find that an evolution of this break of $\nu_{\mathrm{b_1}} \approx 10^{15}$ Hz $\times$ ($t/3.46$ days)$^{-1.32}$ together with an assumed spectral index of $\beta_1 \approx -0.86$ (to match the NuSTAR spectrum) above the break successfully reproduces the X-ray light curve at 1 and 15 keV. An additional break is then needed between the hard X-ray and GeV bands in order to not
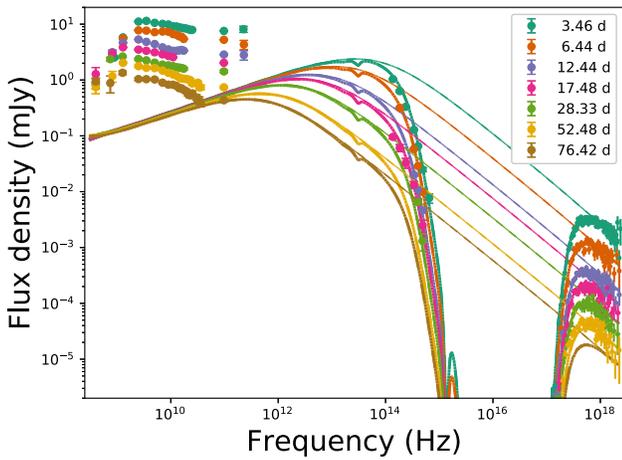
Figure 4. Multiepoch SEDs from our uGMRT, VLA, ALMA, NOEMA, and SMA programs, compared with optical observations and Swift/XRT SEDs at similar times, together with a wind FS model (lines). The FS cannot explain the observed radio flux and slowly evolving radio peak.

overpredict the GeV flux. Fixing the spectral index above this break to $\beta_2 \approx -2$ (from the LAT spectrum), we find that the 1 GeV light curve can be reproduced by a fixed spectral break at $\nu_{b_2} \approx 20.7$ MeV . We plot this model in Figure 6.

While this fiducial, single-component model adequately explains the observations in the centimeter band, X-rays, and at 1 GeV, it underpredicts all optical/NIR observations at $\lesssim 3$ days (just like the physical wind model; see Figure 2) as well as the entire 1.3 mm (SMA) light curve. Furthermore, it does not have any of the temporal breaks that are evident in the 3 mm (97.5 GHz; ALMA and NOEMA) light curve. It is possible that some of these limitations could be resolved by introducing additional, potentially moving breaks into the spectral shape; however, the introduction of these additional degrees of freedom would further reduce the predictive power of the model and make it even more challenging to interpret. Finally, there are no obvious explanations for this particular SED shape or evolution of break frequencies, and thus it is not straightforward to extract meaningful physical information from this model at this stage.

In the scenario that the excess centimeter-band (and possibly millimeter-band) emission arises from a separate population of radiating electrons, potential physical sources for such a component might be (i) a radio SN; (ii) a relativistic Maxwellian population of electrons (i.e., the "nonaccelerated electrons" or "thermal" electrons (Eichler & Waxman 2005; Ressler & Laskar 2017; Warren et al. 2018; Margalit & Quataert 2021); (iii) the RS; and (iv) a two-component jet (i.e., two FS-like regions of different geometries), possibly with energy injection or time-varying microphysical parameters. The radio component is $\gtrsim 100$ times more luminous than the brightest known radio SNe (Figure 7) and peaks significantly earlier ($\sim$few days versus ~ 100 days post-burst); we therefore do not consider emission associated with a possible SN to be a viable explanation for the radio excess in GRB 221009A. The emission spectrum from thermal electrons is expected to be broad and to cut off steeply above the peak (Ressler & Laskar 2017). A detailed test against thermal-electron models was performed by Laskar et al. (2019a) for the low-frequency radio excess in GRB 181201A, and they confirmed that the radio SEDs in that case were narrower than thermal-electron

models would predict. The SEDs observed in this case are similarly sharply peaked, and thus also unlikely to match our current framework of synchrotron radiation from a Maxwellian population of electrons.

In the case of GRB 181201A, the excess radio emission was ultimately ascribed to the RS, albeit with nonstandard parameters. However, the simple power-law fits performed above demonstrate that the temporal evolution of GRB 221009A's radio component is too slow to be ascribed to a RS, even with extreme parameters. To see this, the evolution of the spectral peak[50] ($\nu_{a,r}$) of a Newtonian[51] RS in the regime $\nu_{m,r} < \nu_{a,r}$ is $\frac{\partial \log \nu_{a,r}}{\partial \log t} = -\frac{(15g+24)p + 32g+40}{(14g+7)p + 56g+28}$, where $\Gamma \propto R^{-g}$ is the evolution of the Lorentz factor of the post-shock ejecta with radius (Kobayashi & Sari 2000). We expect $0.5 < g < 1.5$ for a wind environment, but even if we set this aside and consider arbitrarily large values of g (which results in a slower evolution), the expected temporal evolution of the peak frequency asymptotes to $-\frac{15p+32}{14p+56} \approx -0.7$ for the value of $p \approx 1.4$ that is required to match the spectral index above the peak. Similarly, the evolution of the peak flux,[52] $F_{\nu,a,r} = F_{\nu,m,r}\left(\frac{\nu_{a,r}}{\nu_{m,r}}\right)^{(1-p)/2}$. This gives $\frac{\partial \log F_{\nu,a,r}}{\partial \log t} = -\frac{g(15p^2 + 42p - 2) + 4(6p^2 + 14p - 5)}{7(2g+1)(p+4)} \approx -0.94$ for large g and $p \approx 1.4$. Both of these result in a faster-fading SED than observed in the centimeter band for this burst. For completeness, we present sample plots of the RS model in the alternative regime of $\nu_{a,r} < \nu_{m,r} < \nu_{c,r}$ in Appendix B.

Finally, the radio flux cannot be easily ascribed to FS-like emission from a single power-law distribution of electrons either (e.g., in a two-component jet model). This is similar to the scenario explored by Sato et al. (2022; although, as mentioned earlier, their specific model is ruled out by the radio evolution at $\gtrsim 5$ days). For $p \approx 1.4$ for such a model we find that, using the relations of Dai & Cheng (2001) for the regime $1 < p < 2$, we would expect a peak frequency evolution in this case of $\nu_a \propto t^{0.34}$ for a spherical evolution, and $\nu_a \propto t^{0.93}$ for a jet (i.e., post-jet break), together with peak flux evolution of $F_{peak} \propto t^{-1.2}$ and $F_{peak} \propto t^{-1.9}$, respectively, none of which match the observations. On the other hand, while energy injection into the shock producing this emission may arrest the decay of this component, energy injection by itself would not naturally also produce a shallow spectrum above the peak. A combination of both $p < 2$ and energy injection might be a feasible match; however, such a model appears somewhat contrived. Whereas time-varying microphysical parameters could result in a nonstandard evolution of the spectral peak (usually discussed in terms of ν_m, although the peak is at $\nu_a > \nu_m$ here), this would not explain the shallow spectrum above the peak either (Panaitescu & Kumar 2004; van der Horst et al. 2014; Misra et al. 2021).

In summary, to our knowledge, the centimeter and millimeter emission in GRB 221009A do not correspond to the evolution of any standard emission component, including standard prescriptions for forward and RS emission. This is the first time that such a component has been captured in such

---

[50] The peak cannot be $\nu_{m,r}$ or $\nu_{c,r}$, as these evolve as $t^{-1.5}$, which is too fast to match the data.
[51] The emission can decay slower in a Newtonian RS compared to the relativistic RS case.
[52] The spectral index in this expression is not 5/2 due to the definition of $F_{\nu,m,r}$ used here, which corresponds to the non-self-absorbed flux density at $\nu_{m,r}$.
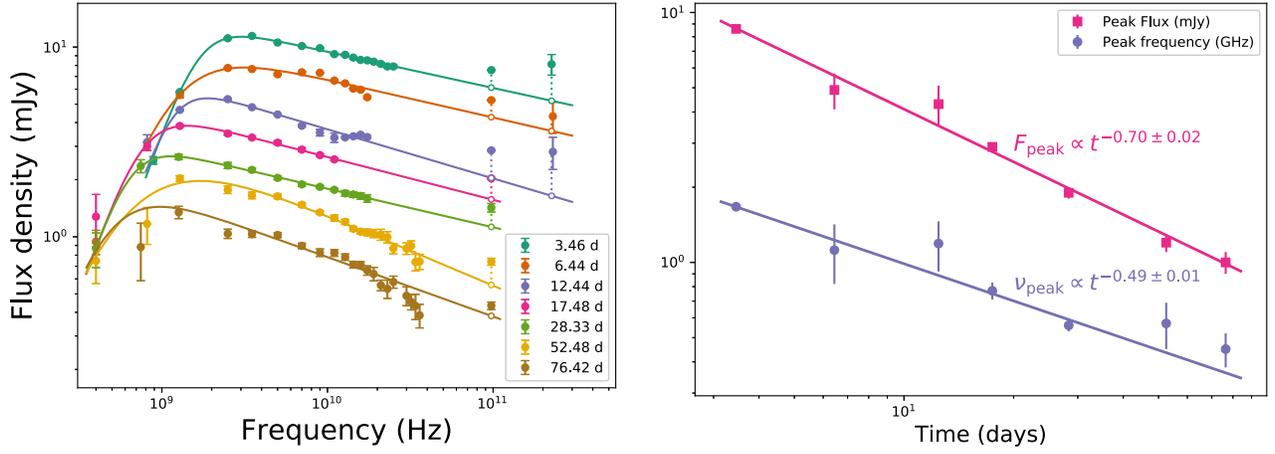
Figure 5. Left: radio SEDs from our uGMRT, VLA, ALMA, NOEMA, and SMA observations reveal a self-absorbed spectrum with a peak at ≈ 2 GHz. The spectral index above the peak is shallow ($\beta \approx -0.2$) with a flattening in the millimeter band ($\gtrsim 100$ GHz), as confirmed by extrapolations (open circles) of broken power-law model fits (lines) to the observations at $\lesssim 50$ GHz. Right: evolution of peak flux and peak frequency from broken power-law fits to the radio SED at $\lesssim 50$ GHz (Table 7).
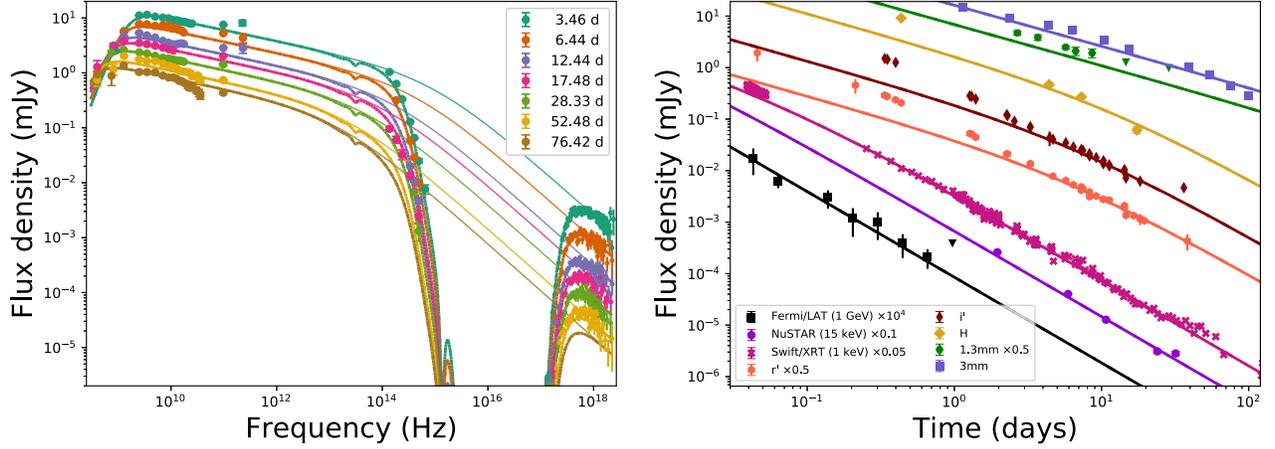
Figure 6. Left: radio to X-ray SEDs (same as Figure 4), together with a fiducial, single-component, broken power-law SED model (lines) where the three break frequencies evolve with time as $\nu_{\mathrm{peak}} \propto t^{-0.49}$, $\nu_{\mathrm{b1}} \propto t^{-1.32}$, and $\nu_{\mathrm{b2}} \propto t^0$, while the peak flux evolves as $F_{\nu,\mathrm{peak}} \propto t^{-0.7}$ (motivated by the observed radio evolution; see Figure 5). The underlying model without the ≈ 4.3 mag of total extinction is shown as thin lines. Right: the corresponding light curves from the GeV to the millimeter band. The model underpredicts the optical observations at $\lesssim 3$ days, the entire 1.3 mm light curve, and does not match any of the temporal breaks seen in the 3 mm light curve.

Table 7
Radio SED Fits and Inferred Outflow Properties

Time (d)	F_{peak} (mJy)	ν_{peak} (GHz)	β_1	β_2	s	R (10^{18} cm)	Γ	E_{min} (10^{48} erg)	B_{eq} (mG)
3.46	8.6 ± 0.2	1.67 ± 0.02	2.5[a]	-0.18 ± 0.01	1.6 ± 0.1	1.40 ± 0.03	9.4 ± 0.1	1.63 ± 0.02	12.43 ± 0.02
6.44	4.9 ± 0.8	1.12 ± 0.30	2.5[a]	-0.20[a]	0.91 ± 0.27	1.43 ± 0.60	6.9 ± 1.4	2.13 ± 0.24	11.9 ± 0.05
12.44	4.3 ± 0.8	1.19 ± 0.25	2.5[a]	-0.26 ± 0.02	1.8 ± 1.2	0.88 ± 0.12	3.9 ± 0.7	4.02 ± 0.51	18.2 ± 0.6
17.48	2.9 ± 0.1	0.77 ± 0.06	2.5[a]	-0.23 ± 0.01	1.4 ± 0.3	1.04 ± 0.11	3.6 ± 0.2	4.28 ± 0.10	12.2 ± 0.1
28.33	1.9 ± 0.1	0.56 ± 0.03	2.5[a]	-0.21 ± 0.01	1.3 ± 0.2	1.00 ± 0.08	2.8 ± 0.1	5.30 ± 0.19	10.99 ± 0.09
52.48	1.2 ± 0.1	0.57 ± 0.12	2.5[a]	-0.37 ± 0.03	0.6 ± 0.1	0.58 ± 0.18	1.5 ± 0.2	7.63 ± 0.45	18.3 ± 0.6
76.42	1.0 ± 0.1	0.45 ± 0.07	2.5[a]	-0.18 ± 0.01	1.0[†]	0.60 ± 0.14	1.3 ± 0.2	9.96 ± 0.68	15.9 ± 0.4

Note.
[a] Fixed. The last four columns list the equipartition radius, Lorentz factor, minimum energy (in the emitting region), and magnetic field, respectively, computed using the formalism of Barniol Duran et al. (2013; see Section 4.2).

exquisite detail; however, previous radio observations of long GRBs have often been sparse, leaving the possibility open that similar emission may be common in long GRBs. We discuss the potential prevalence of such an emission component in radio afterglows of GRBs in Section 4.1.

4. Discussion

4.1. Comparison to other γ-Ray Bursts

We now consider GRB 221009A in the context of the broader GRB population. In the X-ray and γ-ray bands,
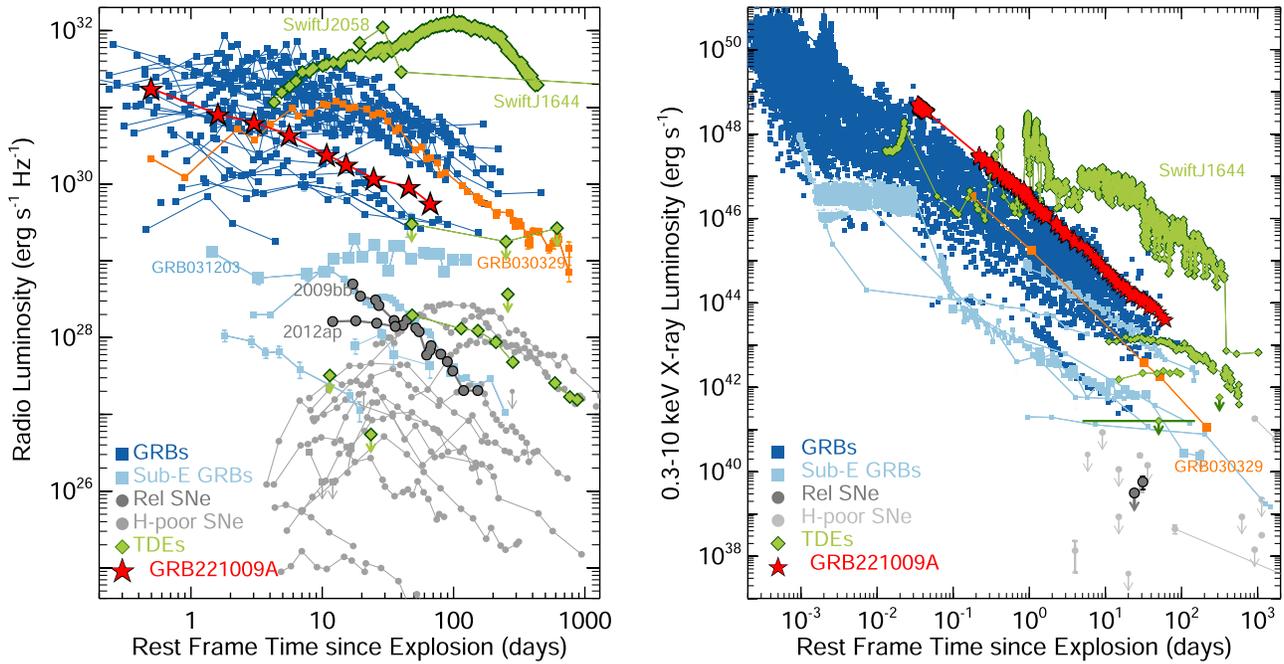
Figure 7. Left: radio spectral luminosity at 8 GHz (rest frame) as a function of rest-frame time for GRBs (deep blue), subenergetic GRBs (light blue), SNe with evidence for relativistic ejecta (dark gray), and hydrogen-poor SNe (light gray). The radio afterglow of GRB 221009A is more luminous than any known radio SN and comparable in luminosity to the afterglows of typical long GRBs. Right: the same plot showing X-ray luminosity in the 0.3–10 keV band. In contrast to the radio, GRB 221009A is one of the most X-ray-luminous GRBs for much of its evolution. Adapted from Margutti et al. (2014).

GRB 221009A is one of the brightest GRBs ever observed (Kennea et al. 2022a; Veres et al. 2022; Ursi et al. 2022; Frederiks et al. 2022; Iwakiri et al. 2022; Kobayashi et al. 2022; Negro et al. 2023). While this is due in part to its proximity, GRB 221009A is also intrinsically among the most luminous known bursts at these wavelengths (Figure 7). Our FS modeling of GRB 221009A suggests that this superlative luminosity is likely not due to an unusually powerful jet but rather to fortuitous geometric alignment: the beaming-corrected jet kinetic energy is average for long GRBs, $E_K = 50.60^{+0.09}_{-0.07}$ erg , but the jet's small opening angle, $\theta_{jet} = 1.64^{+0.28}_{-0.20}$, places it among the most narrowly collimated jets in the GRB population (Laskar et al. 2018). We note that the jet break at ≈130 days in our model is driven by the millimeter-band light curve, and, if a more accurate multiwavelength model can be found that also successfully incorporates the radio and millimeter observations, then this interpretation would likely need to be revisited. Under this FS model, GRB 221009A's kinetic energy is similar to that of other low-redshift GRBs; in particular, it is intermediate between GRB 161219B and GRB 030329 (Figure 8). Given the high γ-ray energy, this implies a relatively high prompt efficiency of $\eta_\gamma \approx 86\%$, independent of the beaming correction.

GRB 221009A is also superlative in the quality and coverage of radio and millimeter data obtained. Despite GRB 221009A's extreme brightness at high energies, its centimeter and millimeter emission is merely average for the GRB population (Figures 7 and 9). It is this combination of extreme X-ray (and optical) luminosity and millimeter mediocrity that makes fitting a FS model to the full data set so challenging: the model overpredicts the millimeter emission at late times unless the millimeter band remains below the peak of the SED, forcing ν_m to remain between the millimeter and optical bands throughout the duration of our observations and requiring a jet break at ≈130 days. Since the inferred narrow collimation angle for this
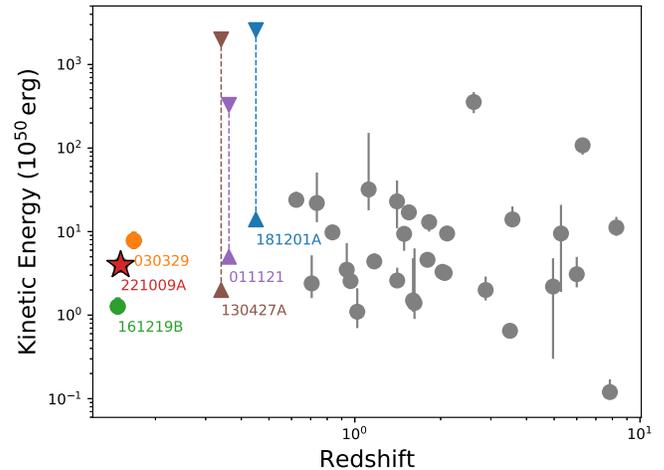
Figure 8. Beaming-corrected kinetic energies of GRBs with multiwavelength data sets and known jet opening angles, as a function of redshift, together with the value of E_K for GRB 221009A derived from our best-fit FS model. The extraordinary brightness of GRB 221009A at high energies may arise from a combination of its proximity and a narrow beaming angle, rather than a high intrinsic E_K.

burst is largely constrained by the millimeter-band light curve, most of which our model cannot explain, a more complete description of the radio emission is also required to derive a more accurate jet opening angle.

Radio observations can also provide unique insight into the physical composition of the jet itself via the detection of RS emission (Laskar et al. 2013; Perley et al. 2014; Laskar et al. 2016; Alexander et al. 2017; Laskar et al. 2019a, 2019b). However, due to the frequent paucity of radio data, deviations of individual data points from this basic picture are often ignored, or attributed to other effects such as interstellar scintillation (e.g., Alexander et al. 2017, 2019;
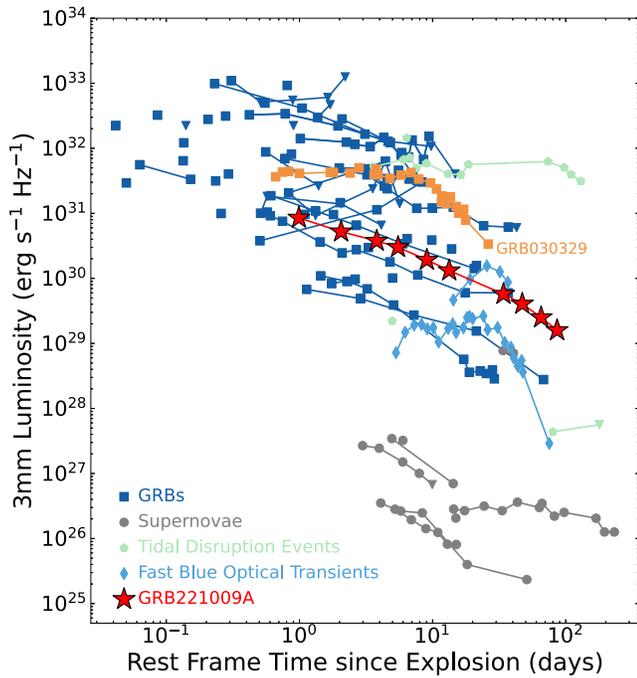
Figure 9. Spectral luminosity of GRB 221009A as a function of rest-frame time in the 3 mm band (red stars), compared to a population of long-duration GRBs (deep blue), SNe (gray), tidal disruption events (light green), and fast blue optical transients (light blue). No K-corrections for variations in intrinsic spectral shape have been applied. The millimeter-band emission from GRB 221009A is a factor of $\approx$5–10 less luminous than GRB 030329 (orange), but of comparable luminosity to that of other GRB afterglows. Adapted from Eftekhari et al. (2022).

Bright et al. 2019). As discussed in Section 3.2 and Appendix B, the exquisite temporal and frequency sampling of the radio data set collected for GRB 221009A rule out a standard RS+FS picture, as well as other commonly considered model extensions (a two-component jet/jet +cocoon, emission from thermal electrons), with high confidence. We attempt to determine if similar behavior could have been previously overlooked in other well-studied radio GRB afterglows in the literature.

Recently, Kangas & Fruchter (2021) systematically considered multiwavelength observations of 21 well-studied long GRBs. They showed that while apparent deviations from a simple FS or FS+RS model in the radio within a single event may not appear statistically significant, when the population is considered as a whole about half of the sample is difficult to explain with a standard afterglow model. Levine et al. (2023) obtained similar results based on a radio-only analysis of a slightly larger sample. In particular, several GRBs in Kangas & Fruchter's (2021) sample (GRB 141121A, GRB 160625B, and GRB 171010A) exhibit shallow radio SEDs at late times, similar to GRB 221009A. Notably, GRB 141121A and GRB 160625B have early radio emission consistent with a standard RS model, but the data are brighter than the models at late times, similar to the issue we faced in attempting to model GRB 221009A's radio emission with a RS. These three GRBs are among the few published events with multifrequency radio coverage extending to such late times, suggesting that broad, slowly evolving radio components like that seen in GRB 221009A may be more common than previously realized, and may occur in GRBs both with and without distinct RS emission at early times.

While the number of GRBs with well-sampled millimeter light curves remains small, several of them also exhibit puzzling behavior relative to other wave bands. For example, GRB 161219B's and GRB 181201A's millimeter light curves were both modeled as the sum of RS and FS emission, but fits to the millimeter light curves in isolation preferred a single power-law decline with a temporal decay rate intermediate between the optical and centimeter bands rather than a broken power law (Laskar et al. 2018, 2019b). Similarly, GRB 221009A's 3 mm light curve evolves as $\sim t^{-1.1}$ at late times—steeper than the low-frequency radio light curves ($\sim t^{-0.7}$ at 1.4 GHz), but shallower than the late-time optical and X-ray light curves. This, together with the centimeter-to-millimeter SED shape, further suggests that the millimeter emission in GRB 221009A may be dominated by yet another separate component, in addition to the FS that dominates the optical and X-rays and the slowly evolving component that dominates the centimeter bands. However, standard synchrotron theory struggles to produce emission that is narrowly peaked enough to dominate the millimeter while remaining subdominant at all other frequencies throughout the duration of our observations.

4.2. Equipartition Analysis of the Radio Component

Assuming that the emission dominating the centimeter bands arises from synchrotron radiation from a shock powered by an outflow, we use energy equipartition arguments to derive estimates of the emission radius, minimum energy, equipartition magnetic field, and bulk Lorentz factor of the emitting region. We employ the formalism of Barniol Duran et al. (2013), assuming area and volume-filling factors of unity, and present our results in Table 7. The emission radius and equipartition magnetic field are roughly constant at $R \approx 10^{18}$ cm and $B \approx 13$ mG, respectively, whereas the bulk Lorentz factor decreases from $\Gamma \approx 9.4$ to $\Gamma \approx 1.3$ between 3.46 and 76.42 days. This is lower than the corresponding bulk Lorentz factor of the FS (which decreases from $\Gamma \approx 73$ to $\Gamma \approx 34$ over the same period), possibly suggesting some structure in the ejecta. The minimum energy increases[53] from $E_{in} \approx 1.6 \times 10^{48}$ erg to $E_{min} \approx 1 \times 10^{49}$ erg over this period.

The apparent decelerating nature of this component yields a lower limit on the Lorentz factor of $\Gamma_0 \approx 9.4$, which corresponds to an upper limit[54] on the ejecta mass of $M_{ej} \approx E_{min}/(\Gamma_0 c^2) \approx 10^{-7} M_\odot$ for $E_{min} \approx 1.6 \times 10^{48}$ erg as derived from the radio SED at 3.46 days, or $M_{ej} \lesssim 6 \times 10^{-7} M_\odot$ as derived from the radio SED at 76.42 days. This is similar in magnitude to the inferred ejecta mass for a typical long-duration GRB with beaming-corrected kinetic energy $E_K \approx 5 \times 10^{50}$ erg (Laskar et al. 2014), assuming a typical initial Lorentz factor of $\Gamma_0 \approx 100$. This indicates that the outflow producing the radio emission in GRB 221009A shares characteristics similar to those of standard long-duration GRBs. However, the stagnant emission

---

[53] In the equipartion framework, this apparent increase in E_{min} is due to deceleration resulting in a greater volume of the emitting plasma becoming visible, with values computed at later epochs providing a stronger constraint on the true minimum energy.
[54] The relationship $E \approx \Gamma M_{ej} c^2$ holds only if the system is still ballistic. If it has been decelerated by the environment (as the stationary radius would indicate), then the Lorentz factor should no longer be connected to the ejecta mass but only to the energy and density. Since the Lorentz factor decreases with time, and because we infer an increasing energy and decreasing Γ, the first epoch yields the tightest constraint and an upper limit on M_{ej}.

radius inferred for this component stands in stark contrast to the expanding outflow expected from standard theoretical models of a relativistic GRB jet propagating in a smooth environment. Finally, the inferred value of the equipartition magnetic field is higher than that inferred for the post-shock B field in the FS ($B \approx 1$ mG$(t/1$ day$)^{-3/4}$), but lower than that inferred for SN shocks in Type Ib/c SNe (Chevalier & Fransson 2006).

4.3. Caveats from Modeling the Forward-shock Emission

We now discuss the mismatch between the FS wind model and the data at multiple wavelengths. The FS model underpredicts the optical emission at $\lesssim 1$ day (Figure 2). Similar excess emission in the past has been attributed to RS emission, although the RS in this case would not match the radio observations (Appendix B). A change in density structure from steep to shallow remains plausible, although the density profile is already steep ($k = 2$) and the density itself already very low ($A_* \approx 2 \times 10^{-3}$). Furthermore, such a transition would also affect the X-rays, which are in the same spectral regime in this model; however, no such transition is apparent in the light curves. Any additional component invoked to explain these optical observations would either need to match the radio SED, or at least not overpredict these. Given the lack of such models, the observed optical excess is puzzling.

The FS model also underpredicts the optical emission at $\gtrsim 30$ days. Excess emission above this model is also apparent in the Swift/XRT light curve at 1 keV in the form of a bump at 30–60 days, and in the final NuSTAR epoch relative to the single power-law fit to the 15 keV light curve (Figure 1). In fact, a similar excess over the broken power-law fits is also apparent in the radio light curves on a very similar timescale (Figure 1), possibly indicative that the radio emission does arise from the same emission region as the X-rays and optical, at least in this narrow time interval. The luminosity of this excess at 11 GHz, the optical i' band, and at 1 keV is $\approx 2 \times 10^{39}$ erg s^{-1}, $\approx 5 \times 10^{41}$ erg s^{-1}, and $\approx 10^{43}$ erg s^{-1}, respectively. The achromatic nature of this bump is suggestive of a hydrodynamic effect, such as the appearance of a counterjet, a second emission component (e.g., cocoon or SN emission), a density enhancement (possibly including an encounter with the wind termination shock), or energy injection. We expect $\Gamma \approx 40$ at ≈ 60 days, so the counterjet possibility appears unlikely. The luminosity of this component is greater than any known SN at each of these wavelengths (Figure 7), making such an origin also unlikely. Previous work on the impact of density enhancements on optical light curves of GRB afterglow suggests that such effects lead to minimal deviations in the light curves owing to the highly relativistic nature of the jet, even if the enhancement is extreme (Nakar & Granot 2007; Uhm & Beloborodov 2007; van Eerten et al. 2009, 2010; Gat et al. 2013; Geng et al. 2014). Whereas energy injection could conceivably create such a signature, it would need to be coupled with a jet break in order for the light curves to not asymptote to a higher flux level. In their study of energy injection in GRBs, Laskar et al. (2015) find that, in three out of four cases studied, the jet breaks were within a factor of ≈ 2 from the end of the period of energy injection. If the observed bumps in the light curve for GRB 221009A are related to energy injection, this would continue such a trend. However, the inability of the FS model to directly connect with the radio observations makes further investigation of this possibility challenging.

The best-fit wind model overpredicts the observed NIR (*JHK*-band) flux by $\approx 15\%$–30%, with the offset worsening with time. On the other hand, no such offset is apparent in the optical fits. We find that this is due to an apparent change in the spectral slope between the NIR and optical bands from $\beta_{\mathrm{NIR-opt}} = -0.76 \pm 0.04$ at ≈ 4.4 days (Section 3.1) to $\beta_{\mathrm{NIR-opt}} = -0.52 \pm 0.04$ at ≈ 17.5 days. Such a hardening of the NIR-to-optical spectrum is unexpected and cannot be understood in the standard synchrotron framework in our preferred spectral regime of $\nu_m \lesssim \nu_{\mathrm{opt}} < \nu_X < \nu_c$. Whereas such a color evolution from red to blue is similar to that expected from the emergence of an underlying SN, inclusion of such a component would overpredict the optical observations. Suppressing the afterglow contribution to both the optical and NIR at this time would require either a steepening of the electron index p with time (which would then affect the X-ray fit) or a faster evolution of ν_m, which would worsen the tension in the millimeter band at ≈ 100 days, making this interpretation untenable. It is also possible that this apparent change in $\beta_{\mathrm{NIR-opt}}$ instead arises from systematic calibration errors in the data. Further investigation of this anomaly requires better light-curve coverage of the NIR afterglow and is beyond the scope of this work.

The model fit appears slightly worse in the LAT 1 GeV band. This is partially due to a slightly shallower decay index: the model predicts $\alpha_{\mathrm{LAT}} = (2-3p)/4 \approx -1.40$, compared to the observed value of $\alpha_{\mathrm{LAT}} \approx -1.47$. It is also in part due to the higher flux in the model (by $\approx 50\%$) compared to the data. The flux offset could be addressed by a slightly lower value of ν_c, or, alternatively, both of these could be remedied by a slightly larger value of p. Since ν_c depends on all four physical parameters, it is nontrivial to discern the origin of additional constraints on its value imposed by the rest of the data. The challenge with a higher value of p, on the other hand, lies in fitting the optical-to-X-ray spectral index; increasing p while keeping the model flux in the X-rays fixed would result in the model overpredicting the NIR even more. Thus, the current value of p is a compromise between strongly overpredicting one or the other of the NIR or GeV emission. Finally, we note that the LAT spectrum shows some evidence for steepening in the last two bins at $\gtrsim 31$ ks ($\gtrsim 0.4$ days). This could be due to the lower photon flux reducing the fluence of the highest-energy photons in this bin. However, if this reduction is real, it could also indicate the movement of the maximum synchrotron frequency, ν_{max}, into the LAT band. We defer the discussion of this potential effect to future work.

Finally, we speculate on a possible unifying underlying cause for some of these issues. One possible way to resolve the tension between our observations and our analytic model might lie in constructing a more realistic distribution of relativistic electron energies. Standard synchrotron theory assumes that the population of radiating electrons are accelerated into a simple power-law distribution of energies with an abrupt low-energy cutoff at γ_{min}, resulting in a spectral break (ν_m). Our current model for GRB 221009A requires ν_m to remain between the millimeter and the optical throughout our observations; we never observe a break in any light curve attributable to the transition of ν_m through that frequency band, although we infer its presence in the optical at $\lesssim 2$ days by dint of the constraint on the flux of the $\nu^{1/3}$ segment imposed by the millimeter-band data at ≈ 100 days. Changing the low-energy end of the relativistic electron distribution would change the SED below

$F_{\rm peak}$, exactly the regime where our current model struggles to reproduce our observations. We defer further exploration of this and other possibilities to future work.

4.4. Synchrotron Self-Compton Predictions

Multiple experiments have reported the detection of VHE photons from GRB 221009A (Dzhappuev et al. 2022; Huang et al. 2022), making GRB 221009A the newest member of the very small class of GRBs with detected VHE emission (GRBs 180720B, 190114C, 190829A, and 201216C; Abdalla et al. 2019; MAGIC Collab 2019; Blanch et al. 2020; H. E. S. S. Collaboration et al. 2021). GRB 221009A also exhibited the highest-energy photon yet associated with any GRB (18 TeV; Huang et al. 2022). Armed with a predictive model, however imperfect, we consider whether these VHE photons could arise from FS emission. Huang et al. (2022) report 5000 VHE photons in the span of $\approx$2000 s following the Fermi/GBM trigger, corresponding to a flux of $\approx 3 \times 10^{-10}$ erg s^{-1} cm^{-2} at 1 TeV (computed assuming a LHAASO collecting area of 1 km^2 and a mean photon energy of $\approx$1 TeV, ignoring spectral corrections). At a time of $\approx$500 s after the burst, we compute both the synchrotron spectrum from our FS model and the corresponding synchrotron self-Compton (SSC) emission expected, the latter by integrating the synchrotron spectrum over an electron distribution back-calculated from the locations of the break frequencies at this time. We find that a synchrotron flux and SSC flux, at 1 TeV, of $\approx 1.2 \times 10^{-8}$ erg s^{-1} cm^{-2} and $\approx 3 \times 10^{-11}$ erg s^{-1} cm^{-2}, respectively. Thus, in the (presumed) absence of a high-energy cutoff in the electron spectrum, the synchrotron spectrum will dominate over SSC at 1 TeV, and hence the intrinsic spectrum is expected to be $\approx -p/2 \approx -1.1$ in F_ν. The synchrotron flux is a factor of $\approx$40 higher than the rough observed flux computed above; absorption due to γ–γ pair production against the extragalactic background light is expected to attenuate the observed spectrum (although, see also Sahu et al. 2023), and this deficit is of the same order of magnitude as, but smaller than, that inferred for GRB 190114C (MAGIC Collab 2019). Thus, it is conceivable that the VHE emission for this GRB was produced by the FS, although a full analysis requires the VHE data. We conclude with two caveats. First, this is only an order-of-magnitude estimate, and have not considered, for instance, a high-energy cutoff in the electron spectrum in this calculation (which could lead to SSC dominating over synchrotron emission in the VHE range). Second, our FS model has several shortcomings, and the true FS model flux at the time of the VHE detection remains somewhat uncertain.

5. Conclusions

We have presented multiwavelength observations of the superlative GRB 221009A, spanning 15 orders of magnitude in frequency and four in time. We find that GRB 221009A's NIR, optical, X-ray, and γ-ray emission can be well modeled as a synchrotron FS from a highly collimated relativistic jet interacting with a low-density, wind-like medium. GRB 221009A's high brightness as observed from Earth can be attributed to a combination of its relative proximity, its large intrinsic luminosity, and, potentially, a high degree of jet collimation combined with an on-axis orientation.

GRB 221009A strongly demonstrates the need for additional theoretical work to fully understand the ultra-relativistic jets

seen in long GRBs. While a simple FS model is broadly consistent with a large fraction of our data, the radio and millimeter emission in particular are difficult to explain within the scope of standard synchrotron theory. We consider two possibilities: (i) that the radio emission is due to an additional synchrotron emission component (with a possible second additional component required to explain the millimeter emission), or (ii) that our basic analytic models of relativistic synchrotron emission need to be modified in some fundamental way. We find that the temporal evolution and spectral shape of the centimeter emission are inconsistent with standard analytic models for FS or RS emission propagating in constant-density or wind-like media. However, the peak frequency and peak flux density of this component evolve simply with time (as $\nu_{\rm peak} \propto t^{-0.5}$ and $F_{\rm peak} \propto t^{-0.7}$, respectively), perhaps suggesting that an analytic description of this component might be possible if a nonstandard assumption is made (e.g., evolving microphysical parameters). While fully exploring extensions to the standard synchrotron afterglow models is beyond the scope of this paper, we briefly speculate that a more realistic treatment of the low-energy end of the relativistic electron distribution may solve some of the issues.

GRB 221009A's proximity means that it will remain detectable with a wide variety of radio facilities for years to come, providing a test bed for future theoretical work and an opportunity to further refine the synchrotron model applied in this paper. In addition, GRB 221009A's radio brightness and longevity will provide rich opportunities for additional science, including directly measuring the physical size of the afterglow with very-long-baseline interferometry observations (previously only convincingly demonstrated for GRB 030329; Taylor et al. 2004) and constraining the magnetic field structure of the jet with polarization observations (such as for GRB 190114C; Laskar et al. 2019b).

Appendix A
An ISM Model

In this section, we consider an ISM model with $p < 2$ in the regime $\nu_c < \nu_{opt} < \nu_X$ with an early jet break ($t_{jet} \approx 0.55$ days) in order to match the optical and X-ray spectral index and light curves, as discussed in Section 3.1. The low value of p is required to match the observed NIR-to-X-ray spectral index of $\beta_{NIR-X} \approx -0.70$ in the stipulated regime of $\nu_c < \nu_{opt} < \nu_X$. We set $p = 1.5$ and tune the parameters to match the output X-ray and optical light curves. To calculate the light curves, we replace $\bar{\epsilon}_e$ in Granot & Sari (2002) by ϵ_e, and note that there will need to be a change in electron spectrum at some high Lorentz factor in order to keep the total energy in accelerated particles finite. In this model, $\nu_c \approx 3 \times 10^{13}$ Hz $< \nu_{opt}$, as required in order to satisfy $\beta_{NIR-opt} \approx \beta_{NIR-X}$ (Section 3.1). We find that in this model the jet becomes nonrelativistic at $t_{NR} \approx 11$ days and the resultant model light curves overpredict the radio SEDs (Figure 10). This is fundamentally because it is not possible to match the radio SED onto the optical with a single synchrotron emission component without invoking additional spectral breaks. Thus, the ISM, single-jet model is ruled out for this burst.
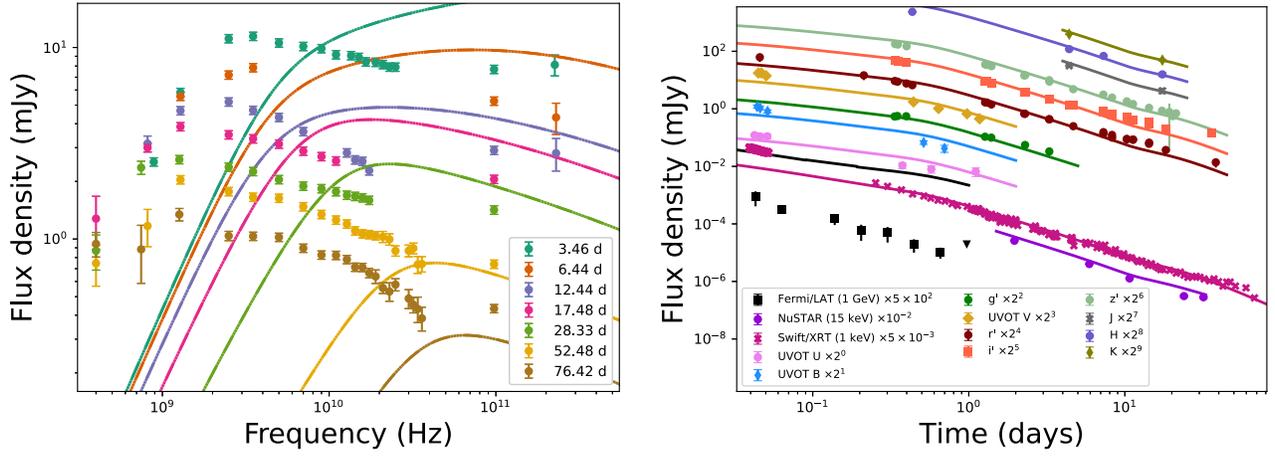
Figure 10. Radio SEDs (left) and light curves (right) for a low-p ISM model with parameters $p = 1.5$, $\epsilon_e = 0.07$, $\epsilon_B = 0.03$, $n_0 = 10$ cm^{-3}, $E_{K,iso} = 1.5 \times 10^{52}$ erg, and $A_{V,host} = 0.3$ mag. This model requires a jet break at $t_{jet} = 0.55$ days (implying $\theta_{jet} = 9°$ and $E_K = 2 \times 10^{50}$ erg) in order to match the X-ray and optical light curves; however, the model significantly overpredicts the millimeter-band observations at $\lesssim 28$ days, overpredicts the Fermi/LAT observations by two orders of magnitude, and does not match the centimeter-band SED at all, and is therefore ruled out.

Appendix B
Newtonian Reverse-shock Model

The excess radio emission described in Section 3.2 cannot be easily ascribed to RS emission. To demonstrate this, we combine the FS model described in Section 3.1 with an RS model with the following parameters: $\nu_{a,r} \approx 2.3 \times 10^9$ Hz, $\nu_{m,r} \approx 1.2 \times 10^{11}$ Hz, and $F_{\nu,m,r} \approx 94$ mJy, selected to achieve an approximate match to the centimeter-band SED at ≈ 17.48 days. The RS cooling break is only weakly constrained to $\nu_{c,r}(1\ \mathrm{day}) \gtrsim 10^{12}$ Hz in this model, so as to not strongly affect

the centimeter-band SED. We also require $p \approx 2$ in order to match the shallow centimeter-band spectral index above the peak at $\gtrsim 2$ GHz. We present a Newtonian RS model with $g = 5$ in Figure 11. A higher value of g leads to a slower RS evolution. For a wind medium, we expect $0.5 \leqslant g \leqslant 1.5$. Even with $g \approx 5$, the evolution of the model SED (with a peak given by $\nu_{m,r}$) is not slow enough to match the observations. A relativistic RS would evolve even faster. Thus, the presently available suite of RS models cannot match the radio observations for this burst.
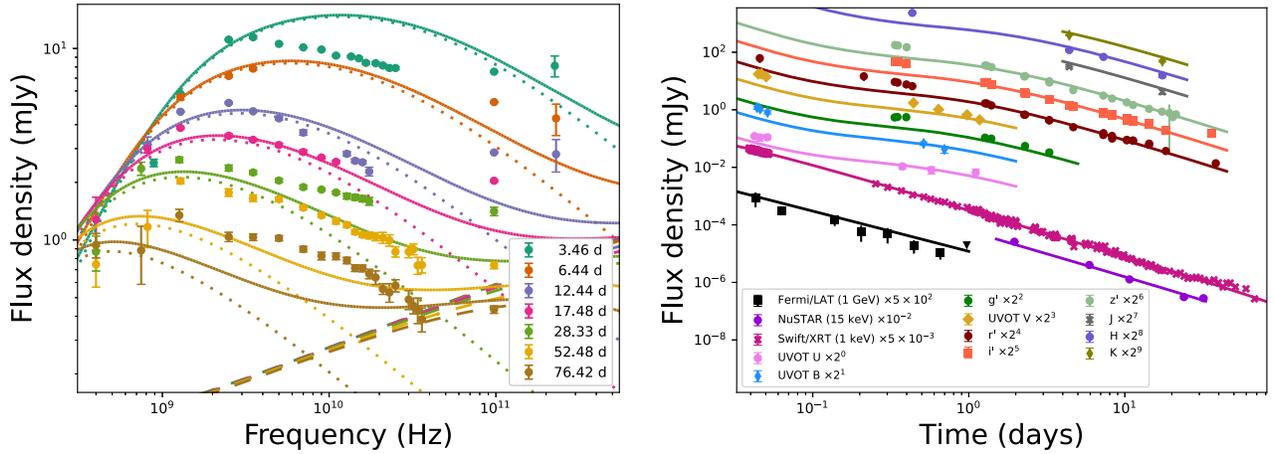

Figure 11. Radio SEDs (left) and light curves (right) for a joint wind model (solid lines) combining a reverse shock (dotted) with the forward-shock model (dashed) described in Section 3.1. This Newtonian RS model with $g \approx 5$ is tailored to roughly match the centimeter-band SED at ≈ 17.48 days. Even with an extreme value of g, the RS model cannot match the rest of the radio data and the early ($\lesssim 1$ day) UV/optical light curves, and is therefore disfavored.

ORCID iDs

Tanmoy Laskar ⓘ https://orcid.org/0000-0003-1792-2338
Kate D. Alexander ⓘ https://orcid.org/0000-0002-8297-2473
Raffaella Margutti ⓘ https://orcid.org/0000-0003-4768-7586
Tarraneh Eftekhari ⓘ https://orcid.org/0000-0003-0307-9984
Ryan Chornock ⓘ https://orcid.org/0000-0002-7706-5668
Edo Berger ⓘ https://orcid.org/0000-0002-9392-9681
Yvette Cendes ⓘ https://orcid.org/0000-0001-7007-6295
Anne Duerr ⓘ https://orcid.org/0000-0003-1716-4119
Daniel A. Perley ⓘ https://orcid.org/0000-0001-8472-1996
Maria Edvige Ravasio ⓘ https://orcid.org/0000-0003-3193-4714
Ryo Yamazaki ⓘ https://orcid.org/0000-0002-1251-7889
Eliot H. Ayache ⓘ https://orcid.org/0000-0002-8225-5431
Thomas Barclay ⓘ https://orcid.org/0000-0001-7139-2724
Rodolfo Barniol Duran ⓘ https://orcid.org/0000-0002-5565-4824
Shivani Bhandari ⓘ https://orcid.org/0000-0003-3460-506X
Daniel Brethauer ⓘ https://orcid.org/0000-0001-6415-0903
Collin T. Christy ⓘ https://orcid.org/0000-0003-0528-202X
Deanne L. Coppejans ⓘ https://orcid.org/0000-0001-5126-6237
Paul Duffell ⓘ https://orcid.org/0000-0001-7626-9629
Wen-fai Fong ⓘ https://orcid.org/0000-0002-7374-935X
Andreja Gomboc ⓘ https://orcid.org/0000-0002-0908-914X
Cristiano Guidorzi ⓘ https://orcid.org/0000-0001-6869-0835
Jamie A. Kennea ⓘ https://orcid.org/0000-0002-6745-4790
Shiho Kobayashi ⓘ https://orcid.org/0000-0001-7946-4200
Andrew Levan ⓘ https://orcid.org/0000-0001-7821-9369
Andrei P. Lobanov ⓘ https://orcid.org/0000-0003-1622-1484
Brian D. Metzger ⓘ https://orcid.org/0000-0002-4670-7509
Eduardo Ros ⓘ https://orcid.org/0000-0001-9503-4892
Genevieve Schroeder ⓘ https://orcid.org/0000-0001-9915-8147
P. K. G. Williams ⓘ https://orcid.org/0000-0003-3734-3587

References

Abdalla, H., Adam, R., Aharonian, F., et al. 2019, Natur, 575, 464
Alexander, K. D., Laskar, T., Berger, E., et al. 2017, ApJ, 848, 69
Alexander, K. D., Laskar, T., Berger, E., et al. 2019, ApJ, 870, 67
Arnett, D. 1996, Supernovae and Nucleosynthesis (Princeton Univ. Press: Springer)
Atwood, W. B., Abdo, A. A., Ackermann, M., et al. 2009, ApJ, 697, 1071
Barniol Duran, R., Nakar, E., & Piran, T. 2013, ApJ, 772, 78
Blanch, O., Longo, F., Berti, A., et al. 2020, GCN, 29075, 1
Bright, J., Rhodes, L., Fender, R., et al. 2022, GCN, 32653, 1
Bright, J. S., Horesh, A., van der Horst, A. J., et al. 2019, MNRAS, 486, 2721
Brivio, R., Ferro, M., D'Avanzo, P., et al. 2022, GCN, 32652, 1
Chevalier, R. A., & Fransson, C. 2006, ApJ, 651, 381
Dai, Z. G., & Cheng, K. S. 2001, ApJL, 558, L109
Dai, Z. G., & Gou, L. J. 2001, ApJ, 552, 72
D'Avanzo, P., Ferro, M., Brivio, R., et al. 2022, GCN, 32755, 1
de Ugarte Postigo, A., Bremer, M., Thoene, C. C., et al. 2022b, GCN, 32676, 1
de Ugarte Postigo, A., Izzo, L., Pugliese, G., et al. 2022a, GCN, 32648, 1
Dichiara, S., Gropp, J. D., Kennea, J. A., et al. 2022, GCN, 32632, 1
Dzhappuev, D. D., Afashokov, Y. Z., Dzaparova, I. M., et al. 2022, ATel, 15669, 1
Eftekhari, T., Berger, E., Metzger, B. D., et al. 2022, ApJ, 935, 16
Eichler, D., & Waxman, E. 2005, ApJ, 627, 861
Evans, P. A., Beardmore, A. P., Page, K. L., et al. 2007, A&A, 469, 379
Evans, P. A., Beardmore, A. P., Page, K. L., et al. 2009, MNRAS, 397, 1177
Ferro, M., Brivio, R., D'Avanzo, P., et al. 2022, GCN, 32804, 1
Foreman-Mackey, D., Hogg, D. W., Lang, D., & Goodman, J. 2013, PASP, 125, 306
Frail, D. A., Metzger, B. D., Berger, E., Kulkarni, S. R., & Yost, S. A. 2004, ApJ, 600, 828
Frederiks, D., Lysenko, A., Ridnaia, A., et al. 2022, GCN, 32668, 1
Fulton, M. D., Smartt, S. J., Rhodes, L., et al. 2023, arXiv:2301.11170
Gat, I., van Eerten, H., & MacFadyen, A. 2013, ApJ, 773, 2
Geng, J. J., Wu, X. F., Li, L., Huang, Y. F., & Dai, Z. G. 2014, ApJ, 792, 31
Granot, J., & Sari, R. 2002, ApJ, 568, 820
Greisen, E. W. 2003, in Information Handling in Astronomy—Historical Vistas, ed. A. Heck, Vol. 285 (Dordrecht: Kluwer), 109
Guarini, E., Tamborra, I., Bégué, D., & Rudolph, A. 2023, arXiv:2301.10256
Harrison, F. A., Craig, W. W., Christensen, F. E., et al. 2013, ApJ, 770, 103
H. E. S. S. Collaboration, Abdalla, H., Aharonian, F., et al. 2021, Sci, 372, 1081
Huang, Y., Hu, S., Chen, S., et al. 2022, GCN, 32677, 1
Huber, M., Schultz, A., Chambers, K. C., et al. 2022, GCN, 32758, 1
Hunter, J. D. 2007, CSE, 9, 90
Iwakiri, W., Jaisawal, G. K., Younes, G., et al. 2022, GCN, 32694, 1
Jeffreys, H. 1946, RSPSA, 186, 453
Jóhannesson, G., Björnsson, G., & Gudmundsson, E. H. 2006, ApJ, 647, 1238
Kale, R., & Ishwara-Chandra, C. H. 2021, ExA, 51, 95
Kangas, T., & Fruchter, A. S. 2021, ApJ, 911, 14
Kann, D. A., & Agui Fernandez, J. F. 2022, GCN, 32762, 1
Kennea, J. A., Tohuvavohu, A., Osborne, J. P., et al. 2022a, GCN, 32651, 1
Kennea, J. A., Williams, M. & Swift Team 2022b, GCN, 32635, 1
Kobayashi, K., Negoro, H., Nakajima, M., et al. 2022, GCN, 32756, 1
Kobayashi, S., Piran, T., & Sari, R. 1997, ApJ, 490, 92
Kobayashi, S., & Sari, R. 2000, ApJ, 542, 819
Kobayashi, S., & Zhang, B. 2003, ApJL, 582, L75
Kumar, P., & Piran, T. 2000, ApJ, 532, 286
Laskar, T., Alexander, K. D., Berger, E., et al. 2016, ApJ, 833, 88
Laskar, T., Alexander, K. D., Berger, E., et al. 2018, ApJ, 862, 94
Laskar, T., Alexander, K. D., Gill, R., et al. 2019b, ApJL, 878, L26
Laskar, T., Berger, E., Margutti, R., et al. 2015, ApJ, 814, 1
Laskar, T., Berger, E., Tanvir, N., et al. 2014, ApJ, 781, 1
Laskar, T., Berger, E., Zauderer, B. A., et al. 2013, ApJ, 776, 119
Laskar, T., van Eerten, H., Schady, P., et al. 2019a, ApJ, 884, 121
Leung, J., Lenc, E., & Murphy, T. 2022, GCN, 32736, 1
Levan, A. J., Barclay, T., Bhirombhakdi, K., et al. 2022, GCN, 32921, 1
Levine, D., Dainotti, M., Fraija, N., et al. 2023, MNRAS, 519, 4670
Lipunov, V., Kornilov, V., Gorbovskoy, E., et al. 2022, GCN, 32634, 1
MAGIC Collab 2019, Natur, 575, 455
Malesani, D. B., Levan, A. J., Izzo, L., et al. 2023, arXiv:2302.07891
Margalit, B., & Quataert, E. 2021, ApJL, 923, L14
Margutti, R., Milisavljevic, D., Soderberg, A. M., et al. 2014, ApJ, 797, 107
Marshall, F. E., Antonelli, L. A., Burrows, D. N., et al. 2011, ApJ, 727, 132
McMullin, J. P., Waters, B., Schiebel, D., Young, W., & Golap, K. 2007, in ASP Conf. Ser. 376, Astronomical Data Analysis Software and Systems XVI, ed. R. A. Shaw, F. Hill, & D. J. Bell (San Francisco, CA: ASP), 127
Mészáros, P., Rees, M. J., & Wijers, R. A. M. J. 1998, ApJ, 499, 301
Misra, K., Resmi, L., Kann, D. A., et al. 2021, MNRAS, 504, 5685
Nakar, E., & Granot, J. 2007, MNRAS, 380, 1744
2014, Nasa High Energy Astrophysics Science Archive Research Center (Heasarc)HEAsoft: Unified Release of FTOOLS and XANADU, Astrophysics Source Code Library, record ascl:1408.004
Negro, M., Di Lalla, N., Omodei, N., et al. 2023, arXiv:2301.01798
O'Connor, B., Troja, E., Dichiara, S., Gillanders, J., & Cenko, S. B. 2022a, GCN, 32750, 1
O'Connor, B., Troja, E., Dichiara, S., Gillanders, J., & Cenko, S. B. 2022b, GCN, 32860, 1
Panaitescu, A., & Kumar, P. 2004, MNRAS, 350, 213
Perley, D. A., Cenko, S. B., Corsi, A., et al. 2014, ApJ, 781, 37
Piran, T. 2005, RvMP, 76, 1143
Rastinejad, J., & Fong, W. 2022, GCN, 32749, 1
Rees, M. J., & Meszaros, P. 1992, MNRAS, 258, 41P
Rees, M. J., & Meszaros, P. 1998, ApJL, 496, L1
Ren, J., Wang, Y., & Zhang, L.-L. 2022, arXiv:2210.10673
Ressler, S. M., & Laskar, T. 2017, ApJ, 845, 150
Rhoads, J. E. 1999, ApJ, 525, 737
Rossi, E., Lazzati, D., & Rees, M. J. 2002, MNRAS, 332, 945
Sahu, S., Medina-Carrillo, B., Sánchez-Colón, G., & Rajpoot, S. 2023, ApJL, 942, L30
Sari, R., & Piran, T. 1999, ApJ, 520, 641
Sari, R., Piran, T., & Halpern, J. P. 1999, ApJL, 519, L17
Sari, R., Piran, T., & Narayan, R. 1998, ApJL, 497, L17
Sato, Y., Murase, K., Ohira, Y., & Yamazaki, R. 2022, arXiv:2212.09266
Sault, R. J., Teuben, P. J., & Wright, M. C. H. 1995, in ASP Conf. Ser. 77, Astronomical Data Analysis Software and Systems IV, ed. R. A. Shaw, H. E. Payne, & J. J. E. Hayes (San Francisco, CA: ASP), 433
Schlafly, E. F., & Finkbeiner, D. P. 2011, ApJ, 737, 103

Shepherd, M. C., Pearson, T. J., & Taylor, G. B. 1994, BAAS, 26, 987

Steele, I. A., Smith, R. J., Rees, P. C., et al. 2004, Proc. SPIE, 5489, 679

Taylor, G. B., Frail, D. A., Berger, E., & Kulkarni, S. R. 2004, ApJL, 609, L1

Team, F. S. S. D. 2019, Fermitools: Fermi Science Tools, Astrophysics Source Code Library, record ascl:1905.011

Uhm, Z. L., & Beloborodov, A. M. 2007, ApJL, 665, L93

Ursi, A., Panebianco, G., Pittori, C., et al. 2022, GCN, 32650, 1

van der Horst, A. J., Paragi, Z., de Bruyn, A. G., et al. 2014, MNRAS, 444, 3151

van Eerten, H. J., Leventis, K., Meliani, Z., Wijers, R. A. M. J., & Keppens, R. 2010, MNRAS, 403, 300

van Eerten, H. J., Meliani, Z., Wijers, R. A. M. J., & Keppens, R. 2009, MNRAS, 398, L63

Veres, P., Burns, E., Bissaldi, E., et al. 2022, GCN, 32636, 1

Warren, D. C., Barkov, M. V., Ito, H., Nagataki, S., & Laskar, T. 2018, MNRAS, 480, 4060

Williams, M. A., Kennea, J. A., Dichiara, S., et al. 2023, arXiv:2302.03642

Woosley, S. E., & Bloom, J. S. 2006, ARA&A, 44, 507

Xu, D., Jiang, S. Q., Fu, S. Y., et al. 2022, GCN, 32647, 1

Zhang, B., & Kobayashi, S. 2005, ApJ, 628, 315

Zhang, B., & Mészáros, P. 2002, ApJ, 571, 876

Zhang, B., & Mészáros, P. 2004, IJMPA, 19, 2385